HHS Public Access

Author manuscript

Cell Rep. Author manuscript; available in PMC 2022 April 07.

Published in final edited form as:

Cell Rep. 2022 March 01; 38(9): 110423. doi:10.1016/j.celrep.2022.110423.

Cholesterol biosynthesis defines oligodendrocyte precursor heterogeneity between brain and spinal cord

Luipa Khandker[1], **Marisa A. Jeffries**[1,6], **Yun-Juan Chang**[2], **Marie L. Mather**[1], **Angelina V. Evangelou**[1], **Jennifer N. Bourne**[3], **Azadeh K. Tafreshi**[4], **Isis M. Ornelas**[1,5], **Ozlem Bozdagi-Gunal**[4], **Wendy B. Macklin**[3], **Teresa L. Wood**[1,7,*]

[1]Department of Pharmacology, Physiology & Neuroscience, New Jersey Medical School, Rutgers University, Newark, NJ 07103, USA

[2]Office of Advance Research Computing, Rutgers University, Piscataway, NJ 08854, USA

[3]Department of Cell and Developmental Biology, University of Colorado School of Medicine, Aurora, CO 80045, USA

[4]Department of Psychiatry, New Jersey Medical School, Rutgers University, Newark, NJ 07103, USA

[5]Present address: Department of Physiological Sciences, Health Sciences Center, Federal University of Espirito Santo, Vitoria-ES, Brazil

[6]Present address: Division of Neurology, The Children's Hospital of Philadelphia, 516D Abramson Center, 3615 Civic Center Blvd, Philadelphia, PA 19104-6030, USA

[7]Lead contact

SUMMARY

Brain and spinal cord oligodendroglia have distinct functional characteristics, and cell-autonomous loss of individual genes can result in different regional phenotypes. However, a molecular basis for these distinctions is unknown. Using single-cell analysis of oligodendroglia during developmental myelination, we demonstrate that brain and spinal cord precursors are transcriptionally distinct, defined predominantly by cholesterol biosynthesis. We further identify the mechanistic target of rapamycin (mTOR) as a major regulator promoting cholesterol biosynthesis in oligodendroglia. Oligodendroglia-specific loss of mTOR decreases cholesterol biosynthesis in both the brain and

*Correspondence: terri.wood@rutgers.edu.

AUTHOR CONTRIBUTIONS

L.K. and T.L.W. conceptualized the project. L.K., M.A.J., M.L.M., I.M.O., A.K.T., and A.V.E. performed experiments and analyzed data. Y.J.C. analyzed single-cell sequencing data. J.N.B. performed electron microscopy. A.K.T. performed callosal slice electrophysiology. L.K., M.A.J., and M.L.M. prepared the figures. L.K. and M.A.J. wrote the manuscript. L.K., M.A.J., Y.J.C., M.L.M., I.M.O., O.B.G., W.B.M., and T.L.W. edited the manuscript.

DECLARATION OF INTERESTS

The authors declare no competing interests.

SUPPLEMENTAL INFORMATION

Supplemental information can be found online at https://doi.org/10.1016/j.celrep.2022.110423.

INCLUSION AND DIVERSITY

We worked to ensure sex balance in the selection of non-human subjects. While citing references scientifically relevant for this work, we also actively worked to promote gender balance in our reference list.

the spinal cord, but mTOR loss in spinal cord oligodendroglia has a greater impact on cholesterol biosynthesis, consistent with more pronounced deficits in developmental myelination. In the brain, mTOR loss results in a later adult myelin deficit, including oligodendrocyte death, spontaneous demyelination, and impaired axonal function, demonstrating that mTOR is required for myelin maintenance in the adult brain.

In brief

Using single-cell RNA sequencing, Khandker et al. reveal that oligodendroglia in the brain and spinal cord are distinct. These differences arise from mechanisms regulating cholesterol acquisition, necessary for maintenance of the lipid-rich myelin sheath, and involve mTOR in the regulation of cholesterol biosynthesis in oligodendroglia.

Graphical Abstract

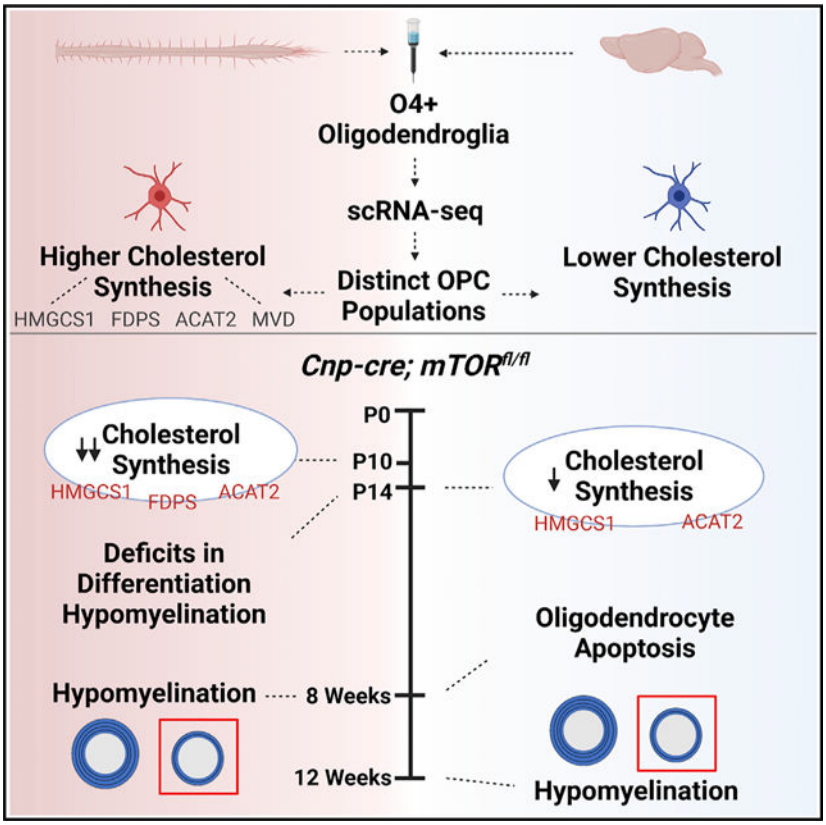

INTRODUCTION

As early as 1921, Del Rio Hortega described oligodendrocytes with distinct morphologies in various regions of the CNS, classifying them into four different categories according to the shape of the cell body and processes and noting where they were found within the CNS (Del Rio-Hortega, 2012; Perez-Cerda et al., 2015). Since then, it has been established that oligodendrocytes and oligodendrocyte precursor cells (OPCs) from different regions of the CNS have distinct origins and are functionally dissimilar, which has implications for

myelination and regenerative capacity (Bechler et al., 2015; Rowitch and Kriegstein, 2010). For example, OPCs from the cortex and spinal cord produce myelin sheaths of different lengths when cultured under similar conditions (Bechler et al., 2015), and transplanted OPCs from white matter differentiate faster than OPCs from gray matter (Vigano et al., 2013). However, the molecular and cellular mechanisms underlying these phenotypic differences are not known. Recent advances in single-cell transcriptomics have revealed heterogeneous oligodendroglial populations, yet no clear functional distinction has been shown between brain and spinal cord oligodendroglia in these reports (Marisca et al., 2020; Marques et al., 2016, 2018).

In addition to distinct developmental origins and cell-intrinsic functional differences in oligodendroglia in brain and spinal cord, lineage-specific gene deletions also can result in altered phenotype between the two CNS regions. The mechanistic target of rapamycin (mTOR) signaling pathway regulates developmental myelination, but the oligodendroglia-specific deletion of *mTOR,* or the mTORC1 binding partner *Raptor,* results in hypomyelination in the spinal cord but not the brain (Bercury et al., 2014; Lebrun-Julien et al., 2014; Wahl et al., 2014). Despite some disruption of myelin gene expression, myelin ultrastructure forms normally in the callosum when *mTOR* or *Raptor* is ablated from developing oligodendroglia (Bercury et al., 2014; Wahl et al., 2014).

Here we define cellular mechanisms that establish distinctions between brain and spinal cord oligodendroglia and demonstrate that during the crucial stage of developmental myelin initiation, oligodendrocyte precursor populations in spinal cord exhibit higher levels of cell-autonomous cholesterol biosynthesis than the equivalent stage precursors in the brain. Conversely, brain oligodendroglia have a higher capacity for extracellular cholesterol uptake. These data support the conclusion that there is a differential requirement for cell-autonomous cholesterol biosynthesis in the brain and spinal cord. We also demonstrate that mTOR promotes cholesterol biosynthesis in oligodendroglia. Thus, the decreased dependence on endogenous cholesterol biosynthesis in brain oligodendrocytes provides a mechanistic basis for why the brain shows fewer deficits in developmental myelination than the spinal cord when mTOR is deleted. However, over time, mTOR loss results in demyelination and axonal dysfunction in the corpus callosum, demonstrating that mTOR is required for myelin maintenance in the adult brain.

RESULTS

Single-cell sequencing of O4^{+} oligodendroglia to analyze regional heterogeneity and effects of mTOR deletion

To investigate oligodendroglial diversity during developmental myelination, we isolated the dynamic population of cells identified by the O4 antigen from mouse brains and spinal cords during active developmental myelination. In the developing rodent CNS, O4 is a cell-surface sulfatide expressed on late-stage OPCs after the early markers platelet-derived growth factor receptor α (PDGFRα) and neural/glial antigen 2 (NG2) are mostly downregulated and which continues to be present on premyelinating as well as actively myelinating oligodendrocytes (Ornelas et al., 2020; Sommer and Schachner, 1981; Warrington and Pfeiffer, 1992). To analyze stage-matched oligodendroglia in the two CNS regions, we

magnetically isolated $O4^+$ cells from spinal cord at postnatal day 10 (P10) and brain at P14, since the spinal cord myelinates earlier than the brain (Foran and Peterson, 1992). These time points correspond to similar developmental phases in the two regions when the most rapid phase of myelination begins (Sturrock, 1980). We used flow cytometry to confirm that the proportions of cells in the P10 spinal cord and P14 brain that had matured to an $O4^+$ stage were similar (64.8% of P10 spinal cord cells are $O4^+$ and 60.3% of P14 brain cells are $O4^+$) (Figures S1A and S1B). We used the 10X Genomics platform for single-cell sequencing of the isolated $O4^+$ oligodendroglia during developmental myelination to (1) reveal transcriptional changes underlying heterogeneity between brain and spinal cord both in normal CNS and after oligodendroglia-specific deletion of mTOR and (2) to define the pathways that require mTOR for cellular functions necessary for terminal maturation and myelination.

Regional heterogeneity: during development, brain and spinal cord precursors are transcriptionally distinct

Unsupervised clustering of control $O4^+$ cells revealed nine distinct populations in developing brain and spinal cord (Figure 1A). The cellular identities of these nine clusters were determined (Figure S2) by matching the top five differentially expressed genes in each cluster to two reference databases (Marques et al., 2016; Zhang et al., 2014). We determined that the clusters form a differentiation continuum of two OPC populations (clusters 7 and 8), two committed OPC (COP) populations (clusters 6 and 0), a population transitioning from COP to newly formed oligodendrocytes (NFOLs) (cluster 1), an NFOL population (cluster 3), a myelin-forming oligodendrocyte (MFOL) population (cluster 4), a population transitioning from MFOL to mature oligodendrocytes (MOLs) (cluster 5), and finally an MOL population (cluster 2) (Figures 1A, S1E, and S2). Our clustering data indicated that the overall distribution of oligodendroglial cell populations was comparable between the isolated brain and the spinal cord $O4^+$ cells (Figure S1F). There was a minor shift toward more precursors (OPCs and COPs) in the brain (12.7% difference), equivalent proportions of NFOLs and MFOLs in the two CNS regions, and a small shift toward more MOLs in the spinal cord (11.2% difference). These data support the conclusion that the two regions are closely stage matched in terms of oligodendroglial differentiation.

The MOL cells (cluster 2) expressed *Mal* and *Trf (transferrin)* (Figure S1G), genes whose products are important for myelination (de los Monteros et al., 1999; Schaeren-Wiemers et al., 2004), as well as *Gsn (gelsolin)* and *Stmn1 (stathmin),* which destabilize the actin cytoskeleton or microtubules, respectively (Liu et al., 2003; Richter-Landsberg, 2008). Since actin deploymerization promotes myelin wrapping (Zuchero et al., 2015), we hypothesized that cluster 2 consisted of oligodendrocytes that were actively wrapping axons. Interestingly, cluster 2 shared transcriptomic similarity with multiple MOL clusters previously identified in the adult CNS (Marques et al., 2016), instead of corresponding to a single population (Figures S2B and S2C), indicating a population of MOL uniquely present during the myelin initiation phase of development.

Figure 1B identifies cells on a uniform manifold approximation and projection (UMAP) plot originating from brain or spinal cord. Despite several studies that have shown cell-intrinsic

regional heterogeneity of oligodendroglia, single-cell studies to date have not found clear distinctions between the brain and the spinal cord (Bechler et al., 2015; Crawford et al., 2016; Marques et al., 2016, 2018). In contrast, we observed that clusters 7 (OPC) and 6 (COP) were primarily composed of cells from the spinal cord, whereas clusters 8 (OPC) and 0 (COP) were almost exclusively brain oligodendroglia (Figure 1B). Cells in cluster 1 (NFOL stage of maturation) did not cluster distinctly based on region. Similarly, brain and spinal cord cells overlapped completely in clusters 3, 4, 5, and 2. The differentiation trajectory of $O4^+$ clusters was consistent with previous single-cell oligodendroglial studies (Marques et al., 2016); however, unlike earlier studies (Bechler et al., 2015; Crawford et al., 2016; Marques et al., 2016, 2018), we identified distinctions between brain and spinal cord precursors in postnatal mice. It is likely that stage matching the two regions and analyzing a dynamic developmental time point enabled detection of regional heterogeneity in our study.

To determine transcriptional differences underlying the distinct precursor populations of brain and spinal cord, we compared clusters 8 and 0 (brain OPCs and COPs) with clusters 7 and 6 (spinal cord OPCs and COPs) and analyzed the differentially expressed genes using Ingenuity Pathway Analysis (IPA). The top five pathways representing the most significant differences between brain and spinal cord precursors were associated with cholesterol biosynthesis (Figures 1C, S3A, and S4A, Table S1, related to Figure 1). Strikingly, genes within all five of these differentially expressed pathways had significantly lower expression in the brain.

The top differentially expressed cholesterol biosynthesis genes comparing brain and spinal cord precursors (clusters 8 and 0 versus clusters 7 and 6) are shown in Figures 1D and 1E. All genes had lower expression in brain compared with spinal cord. These genes included a number of key regulators, such as *Hmgcs1,* which encodes the first enzyme in the cholesterol synthesis pathway and showed the largest expression difference between brain and spinal cord. To determine whether the difference in cholesterol biosynthesis gene expression persisted in more mature cells, brain oligodendrocytes (brain cells in clusters 1, 3, 4, 6, and 2) were compared with spinal cord oligodendrocytes (spinal cord cells in clusters 1, 3, 4, 6, and 2) (Table S2, related to Figure 1). All of the genes maintained lower expression in brain oligodendrocytes compared with spinal cord oligodendrocytes, although the average log fold change (logFC) was greater between the precursor populations (Figures 1D and 1E). A complete list of cholesterol biosynthesis genes and differential expression is included in Figure S3C.

We identified additional pathways contributing to the divergence between brain and spinal cord precursors (OPCs and COPs). We found that after cholesterol biosynthesis, the next differentially regulated pathways were cytoskeletal dynamics and protein kinase A signaling (Figure S3G). The genes in these pathways were also differentially expressed between brain and spinal cord oligodendrocytes (NFOLs, MFOLs, and MOLs) with similar differences in precursors and oligodendrocytes (Figures S3H and S3I). We concluded that, while other pathways also contribute to differences between brain and spinal cord oligodendroglia, cholesterol biosynthesis is the major pathway that differentiates OPCs between the two regions.

To determine whether the difference in cholesterol biosynthesis gene expression between brain and spinal cord oligodendroglia resulted in differential expression of the corresponding enzymes, we measured protein expression in isolated $O4^+$ cells from P10 spinal cord and P14 brains. Hmgcs1 and Fdps showed the largest differences at the transcript level (Figure 1E) and were included for protein expression analysis along with HMGCR, because it is considered the rate-limiting enzyme of cholesterol biosynthesis. Mvd and Acat2, which showed differential transcript expression, were also analyzed at the protein level. HMGCS1, FDPS, MVD, and ACAT2 all had significantly lower protein expression in brain compared with spinal cord oligodendroglia (Figures 2A and 2B). Although decreased at the RNA level, HMGCR protein expression was not significantly different in oligodendroglia from the two regions. To rule out the possibility that the lower expression of cholesterol enzymes was due to a less mature state of the cells in the brain versus spinal cord, we isolated brain $O4^+$ cells at P18 and found that the brain cells continued to have lower expression of HMGCS1 and FDPS even at a later developmental stage (Figure S3D). As cholesterol is an essential, rate-limiting component of the myelin sheath, our findings raise the question of how brain oligodendroglia successfully myelinate despite low expression of cholesterol biosynthesis enzymes. We hypothesized that brain oligodendroglia have an increased capacity for cholesterol uptake compared with spinal cord oligodendroglia. Our single-cell sequencing data showed that *Low-density lipoprotein receptor-related protein-1 (Lrp1),* which functions in receptor-mediated cholesterol uptake in oligodendroglia (Lin et al., 2017), was more highly expressed in brain precursors than in spinal cord precursors (Figure 2C). To determine whether LRP1 protein is also differentially expressed, we measured LRP1 expression in isolated $O4^+$ cells from P10 spinal cord and P14 brains (Figure 2D). LRP1 had significantly higher expression in brain compared with spinal cord oligodendroglia, which was maintained at additional time points (Figure S3E), suggesting increased capacity for cholesterol uptake. We conclude that brain and spinal cord OPCs and COPs are transcriptionally distinct, and that the main contributing pathways are those associated with cholesterol biosynthesis.

To determine the signaling pathway regulating differential cholesterol biosynthesis, we measured mTOR activity in brain and spinal cord oligodendroglia, since the mTOR pathway is known to drive CNS myelination (Bercury et al., 2014; Lebrun-Julien et al., 2014; Wahl et al., 2014). We measured phosphorylation of S6RP, a downstream target of mTOR, in brain and spinal cord $O4^+$ cells and found higher levels in spinal cord compared with the brain (Figure S3F). A recent report demonstrated that S6RP activation in differentiating oligodendrocytes correlates with the peak of myelination in both brain and spinal cord, but no comparison was made on the relative activation in each region (Benardais et al., 2022). We next asked whether brain and spinal cord oligodendroglia respond differently to the loss of mTOR at the transcriptome level.

Oligodendroglial loss of mTOR results in expansion of a population with dysregulated global pathways

To investigate the role of mTOR in the transcriptomic differences between brain and spinal cord $O4^+$ cells, we performed single-cell sequencing in a mouse model with oligodendrocyte-specific knockdown of mTOR (mTOR cKO) in the CNS, using Cre-

recombinase driven by the 2′,3′-cyclic nucleotide 3′-phosphohydrolase (CNP) promoter (see STAR Methods for further details). To visualize population shifts caused by deletion of mTOR, we reclustered the cells from control samples with mTOR cKO cells as described above (Figures 3A and S5A). Each cluster was identified using the top five differentially expressed genes for each cluster (Figures S5C and S5D) and referencing published databases (Marques et al., 2016; Zhang et al., 2014) as for the previous analyses. Similar to the UMAP of control brain and spinal cord, clusters reflected progression along a differentiation continuum from OPCs to COPs to NFOLs to MFOLs and finally to MOLs (Figures 3A and S5B). The clear distinctions between brain and spinal cord precursors (Figure 1B) were masked when all samples are combined; this can be attributed to a greater difference in gene expression between control and mTOR cKO cells than between control brain and control spinal cord.

Separating the UMAPs by CNS region allowed us to visualize population shifts resulting from loss of mTOR within each region (Figure 3B). Although several clusters were altered with deletion of mTOR (Figure 3C), MFOL cluster 7 showed the largest population shift. In the spinal cord this represented an expansion from 0.3% of control $O4^+$ cells to 18.7% of mTOR cKO $O4^+$ cells in cluster 7; in the brain cluster 7 exhibited a smaller expansion from 0.2% of control to 2.9% of mTOR cKO (Figure 3D).

We performed pseudotime analysis to identify the origin of cluster 7 cells. Our data indicated that in control oligodendroglia, MFOL cluster 2 progressed to MOL cluster 1 (Figure S6B). In mTOR cKO oligodendroglia, cluster 2 branched to both cluster 1 and cluster 7 (Figures 3E and S6C). Comparing cluster 7 to its origin, cluster 2, revealed that the top altered pathways were in one of five categories: mTOR signaling, mitochondrial function, apoptotic pathways, cytoskeletal dynamics, and cholesterol biosynthesis (Figures 3F and S4B). Dysregulation of mTOR signaling was to be expected in a population that was almost exclusively present in mTOR cKO. These findings are consistent with previous studies showing specific mTOR-regulated cytoskeletal targets in developing oligodendroglia *in vitro* and *in vivo* during both early stages of morphological differentiation and later stages of myelin wrapping (Musah et al., 2020; Tyler et al., 2011). Cytoskeletal dynamics are essential as MFOLs mature to MOLs and must shift from promoting process extension, requiring microtubule and actin polymerization, to initiating axon wrapping, requiring depolymerization (Brown et al., 2021; Brown and Macklin, 2020; Domingues et al., 2018; Nawaz et al., 2015; Zuchero et al., 2015). Our differential expression data suggested that cluster 7 cells would be unable to undergo the morphological changes necessary for terminal differentiation and initiation of axon wrapping (Figure S6D). Instead of lower expression of *Fyn,* which is downregulated in MOLs (Klein et al., 2002; Marques et al., 2016; Zhang et al., 2014), cells in cluster 7 had higher *Fyn* expression than cells in cluster 2. In contrast, *Gsn,* which functions in actin severing, is normally upregulated as an oligodendrocyte progresses from MFOL to MOL (Marques et al., 2016; Zhang et al., 2014; Zuchero et al., 2015) as seen in cluster 1 (supplemental information) but was downregulated in cluster 7. These data are consistent with impaired initiation of myelination and hypomyelination observed in mTOR cKO developing spinal cord (Musah et al., 2020; Wahl et al., 2014).

mTOR loss dysregulates global pathways important for oligodendrocyte biology

Loss of mTOR in developing oligodendroglia caused dysregulation of genes involved in mitochondrial function, apoptotic pathways, and cholesterol biosynthesis based on cluster 7 analyses (Figure 3F). These pathways are important for normal oligodendrocyte development and function but have not previously been identified as mTOR regulated in oligodendroglia. Next, we compared all mTOR cKO clusters with all control clusters from spinal cord and identified 61 pathways that were altered; the top five pathways are shown in Figures 4A and S4C. Similar to cluster 7, mTOR signaling was dysregulated overall in mTOR cKO spinal cord oligodendroglia. The remaining four pathways, the superpathway of cholesterol biosynthesis, the superpathway of GGDP biosynthesis I, the mevalonate pathway, and cholesterol biosynthesis I, are all associated with cholesterol biosynthesis (Figure S3A).

A similar comparison of all mTOR cKO clusters with all control clusters from brain revealed 20 global pathways dysregulated in mTOR cKO brain $O4^+$ cells. As in the spinal cord, mTOR signaling was one of the top five pathways (Figures 4B and S4D). The superpathway of cholesterol biosynthesis was also dysregulated in the mTOR cKO brain, but less severely than in the spinal cord, with fewer downregulated genes. Genes involved in oxidative phosphorylation, a mechanism for ATP synthesis in the mitochondria, were also dysregulated in mTOR cKO brains.

The remaining top pathways dysregulated in the brain were clathrin-mediated endocytosis signaling, which functions in the internalization of molecules from the plasma membrane into intracellular compartments, and iron homeostasis signaling, which regulates iron uptake, storage, and export. While both pathways have independent functions important for oligodendrocyte biology, they are also associated with cholesterol homeostasis (Mahley, 1988; Todorich and Connor, 2004). To determine whether the transcriptomic changes observed in mTOR cKO are due exclusively to the expansion of MFOL cluster 7, we excluded cluster 7 and compared the remaining mTOR cKO cells with control cells and found that global pathways, including mTOR signaling, remained dysregulated (Figures S6E and S6F). We also considered the possibility that loss of mTOR completely prevents oligodendrocytes from progressing past the MFOL stage, resulting in the expansion of cluster 7 and a lack of MOLs with mTOR deletion. The MOL clusters from mTOR cKO would then be expected to consist of unrecombined cells with intact mTOR and normal mTOR signaling and cholesterol biosynthesis. To address this, we analyzed genes differentially expressed in mTOR cKO cells exclusively within MOL clusters 1 and 6 (Figures S6G and S6H). mTOR signaling was dysregulated in mTOR cKO MOLs, indicating that these cells have not escaped mTOR deletion. Moreover, cholesterol biosynthesis was also dysregulated, demonstrating a continued deficit in mTOR cKO MOLs.

Since dysregulation of cholesterol biosynthesis and oxidative phosphorylation were identified in cluster 7 as well as in mTOR cKO overall, we performed Seahorse functional assays to validate alterations in these pathways with loss of mTOR. Our results indicate that, while mTOR regulates oxidative phosphorylation (Figures S8A and S8B), oligodendrocytes can withstand a small reduction in respiratory capacity without significant effects on myelin gene expression (Figures S8C and S8D). Moreover, based on the similar oxygen

consumption phenotypes in brain and spinal cord, it seems unlikely that this accounts for the greater effect of mTOR loss on spinal cord oligodendroglia in the mTOR cKO.

mTOR is necessary for normal cholesterol biosynthesis in oligodendroglia

To further investigate mTOR regulation of cholesterol biosynthesis gene expression, we treated differentiating primary OPCs in culture with the mTOR inhibitor rapamycin and measured mRNA expression of *Hmgcr, Hmgcs1*, and *Fdps* (Figure 4C), which were among the genes of the cholesterol biosynthesis pathway downregulated in mTOR cKO (Figures 4A and 4B). Inhibiting mTOR significantly decreased expression of all three cholesterol biosynthesis genes, indicating that mTOR is necessary for their normal expression in oligodendroglia. Next, we assessed protein expression of HMGCR, HMGCS1, FDPS, and ACAT2 in $O4^+$ cells isolated from control and mTOR cKO spinal cord (P10) and brain (P14) (Figures 4D and 4E). While HMGCR expression was unaffected in mTOR cKO brain and spinal cord, HMGCS1, FDPS, and ACAT2 expression was significantly reduced in mTOR cKO spinal cord. In the brain, mTOR deletion led to a significant reduction in HMGCS1 in oligodendroglia (27% decrease), although the reduction was less than in spinal cord (52% decrease). Similarly, ACAT2 was reduced in mTOR cKO brain, but with a smaller decrease than in mTOR cKO spinal cord. FDPS was unaffected in the developing brain with deletion of mTOR. We concluded that mTOR deletion dysregulates cholesterol biosynthesis enzymes in both brain and spinal cord oligodendroglia but has a greater impact in the spinal cord. To determine whether reduction of cholesterol enzymes lowered cholesterol production, we directly measured cholesterol levels in freshly isolated $O4^+$ oligodendroglia. Total cholesterol was significantly reduced in both mTOR cKO spinal cord and brain $O4^+$ cells (Figures 4F and 4G) and similar reductions between control and mTOR cKO were maintained at P18 (data not shown). Consistent with the relative reduction of cholesterol biosynthesis enzymes, loss of mTOR reduced cholesterol content to a greater extent in spinal cord than in brain. We directly compared brain and spinal cord cholesterol content at P18 and found that loss of mTOR results in lower cholesterol in brain compared with spinal cord (Figure 4H). These findings demonstrate that mTOR promotes expression of cholesterol biosynthesis enzymes, at both the transcript and the protein level, and maintains normal cholesterol content.

Cholesterol is an integral component of the myelin sheath, and decreased cholesterol biosynthesis via pharmacological inhibition *in vivo* or genetic mutation can cause myelin deficits in both the PNS and the CNS (Saher et al., 2011). Treating primary rat OPCs *in vitro* with simvastatin, an inhibitor of HMGCR, directly affected oligodendrocyte viability (Figure S7A). Since most primary oligodendroglia after 3 and 5 days under differentiation conditions are postmitotic, the reduced cell number from simvastatin treatment was likely due to cell death. Previous studies have shown that simvastatin reduces expression of the myelin proteins CNP, MBP, MAG, and MOG in primary rat OPCs (Smolders et al., 2010). We expanded on these studies and determined that inhibiting cholesterol biosynthesis in primary oligodendroglia with simvastatin reduced myelin gene expression, with higher concentrations and longer treatments having a greater effect (Figures S7B–S7E). Our findings are consistent with reports that simvastatin administration *in vivo* affects oligodendrocyte numbers and MBP expression during remyelination (Miron et al., 2009)

and further demonstrate that inhibiting cholesterol biosynthesis has a cell-autonomous effect on oligodendrocyte viability and on expression of essential myelin genes.

Deficits in cholesterol biosynthesis persist at 8 weeks of age, myelin protein expression is downregulated, and mTOR cKO brain oligodendroglia undergo apoptosis

Our data show that oligodendroglia in the mTOR cKO spinal cord have a greater reduction in cholesterol biosynthesis enzymes and cholesterol content than mTOR cKO brain oligodendroglia. This is consistent with the hypomyelination observed in mTOR cKO spinal cord, whereas the brain shows normal developmental myelination (Wahl et al., 2014). However, it is possible that the lower cholesterol in brain oligodendroglia due to loss of mTOR results in a delayed myelin phenotype.

To determine whether cholesterol biosynthesis enzymes remained reduced in adult brains, we analyzed microdissected corpus callosum of control and mTOR cKO mice at 8 weeks of age. mTOR cKO corpus callosum exhibited a significant reduction in protein expression of both HMGCS1 and FDPS but not HMGCR (Figures 5A and 5B). We also found that expression of both MBP and PLP was significantly reduced in the corpus callosum at 8 weeks (Figure 5C), revealing effects on myelin proteins similar to those observed *in vitro* (Figures S7B–S7E). In addition, immunostaining for MOG revealed a reduction in the area of MOG positivity in the corpus callosum of mTOR cKO animals (Figure 5D) compared with controls.

Our *in vitro* studies indicate that reduced cholesterol biosynthesis can reduce oligodendrocyte viability in brain OPCs (Figure S7A). Furthermore, apoptotic pathway genes are dysregulated in cluster 7, the population of cells expanded in mTOR cKO (Figure 3F). Therefore, to determine whether oligodendrocyte survival is affected *in vivo,* we quantified the number of cleaved caspase-3^+ cells and $SOX10^+$ cells in mTOR cKO and control corpus callosum (Figure 5E). The number of $SOX10^+$ oligodendroglia was reduced in the corpus callosum of mTOR cKO mice, and a corresponding increase in cleaved caspase-3^+/$SOX10^+$ cells indicated that mTOR deletion resulted in apoptosis and loss of oligodendroglia in the brain by 8 weeks of age.

Delayed myelin loss in mTOR cKO brains

Our data suggest that, although developmental myelination in the mTOR cKO brain is structurally normal by electron microscopy (EM) at 8 weeks (Wahl et al., 2014), myelin sheath integrity may be compromised after initial wrapping. Although most developmental myelination is complete by 8 weeks of age in mice, there is continual myelin accumulation between 8 and 12 weeks (Hammelrath et al., 2016). Moreover, loss of oligodendrocytes in the adult corpus callosum might have a further impact on myelin integrity. At 12 weeks of age, mTOR cKO mice exhibited significantly reduced MBP and PLP expression compared with controls (Figure 6A). Immunostaining for MOG also revealed a significant reduction in the area of MOG positivity in mTOR cKO (Figure 6B). These data suggested a progressive myelin deficit from 8 to 12 weeks of age. Analyzing corpus callosal myelination at 12 weeks by EM (Figures 6C–6F), we found fewer myelinated axons (Figure 6D) and thinner myelin by g-ratio analysis (Figure 6E) in mTOR cKO. Both linear regression analysis

(Figure 6E) and g-ratio distribution analysis (Figure 6F) revealed shifts toward higher g-ratio values. To determine whether hypomyelination in mTOR cKO brains recovers with time, we analyzed corpus callosum myelination at 12 months of age and found that thinner myelin persisted in mTOR cKO (Figures S9A–S9C). Taken together with the increased apoptosis at 8 weeks, our data indicate that mTOR deletion from the oligodendrocyte lineage results in oligodendrocyte death and demyelination in the adult brain.

The demyelination that occurs in the brain of the mTOR cKO mice from 8 to 12 weeks could be due either to adult myelin maintenance deficits or to developmental alterations that do not manifest until after 8 weeks. To determine an effect on myelin maintenance, we deleted mTOR specifically from MOLs using inducible *Plp-Cre*^{ERT}*;mTOR*$^{fl/fl}$ adult mice (Plp-mTOR cKO). Myelin analyses revealed deficient long-term myelin maintenance 12 months after mTOR deletion but did not entirely recapitulate the more dramatic phenotype observed in Cnp-mTOR cKO brains at 12 months of age (Figures S9D–S9F). These data indicate that mTOR likely has distinct and necessary functions in brain oligodendroglia during development and in adult myelin maintenance.

Developmental loss of mTOR disrupts nodal structures and axonal function in the adult corpus callosum

Demyelination in diseases such as multiple sclerosis (MS) results in progressive neuronal degeneration and functional deficits. Given the significant myelin loss detected in 12-week corpus callosum, we hypothesized that mTOR cKO mice would have compromised axonal function. To determine whether mTOR cKO brains have disrupted nodal structures, we performed immunostaining for contactin-associated protein 1 (CASPR), a component of paranodes, and NaV1.6, a voltage-gated sodium channel present in nodes of Ranvier (Figure 7A). We observed a significant reduction in the number of paranode-node structures (defined as CASPR-NaV1.6-CASPR) in the midline callosum of mTOR cKO compared with control, suggesting that axonal function may be altered with mTOR loss in oligodendrocytes. To address this directly, we performed compound action potential (CAP) recordings in the midline callosum of coronal slices from 13-week mTOR cKO and control brains (Figure S9G). Representative traces revealed clear differences in CAP response (Figure 7B), with a complete loss of the N1 (myelinated fiber) response and altered N2 (unmyelinated fiber) response in the mTOR cKO callosum. The N1 amplitude was completely absent in mTOR cKO even at the highest stimulation intensity used, while there was a clear N1 response in the control brains (Figure 7C). While latency to N2 response was unchanged in mTOR cKO corpus callosum (Figure 7E), we observed an increased duration of the N2 response (Figure 7F), suggesting changes in the unmyelinated axon response to stimulation. However, the N2 amplitude of the CAP recordings was unchanged across increasing stimulation intensities, indicating that the number of axons is not reduced (Figure 7D). These data indicate that the endogenous demyelination observed in the mTOR cKO callosum results in significantly impaired myelinated and unmyelinated axonal function in adults, despite the lack of obvious axonal damage (Figure S9H).

DISCUSSION

Here we reveal that oligodendrocyte precursors in the brain and spinal cord are transcriptionally distinct. Brain precursors have lower cell-autonomous cholesterol biosynthesis and higher expression of Lrp1 compared with spinal cord precursors. mTOR, a major regulator of CNS myelination, promotes cholesterol biosynthesis in oligodendroglia, and loss of mTOR results in differential expansion in brain and spinal cord of a distinct population of MFOLs with reduced cholesterol biosynthesis and dysregulated cytoskeletal dynamics. This demonstrates that mTOR loss has differential effects on distinct oligodendroglial populations. Normal cholesterol biosynthesis is necessary for oligodendrocyte viability and myelin gene expression *in vitro.* Despite a higher potential for receptor-mediated cholesterol uptake compared with spinal cord oligodendroglia, brain oligodendroglia display decreased cholesterol levels with loss of mTOR. At 8 weeks of age, along with continued reduction of cholesterol biosynthesis, there is increased apoptosis, resulting in fewer brain oligodendroglia in mTOR cKO mice *in vivo.* By 12 weeks of age, mTOR cKO mice exhibit callosal demyelination and impaired axonal function.

The complete abrogation of the N1 response seen in the mTOR cKO corpus callosum at 12 weeks is striking, given that some myelinated axons remain in the corpus callosum based on EM analysis; however, there are potential explanations for this finding. The first possibility is that the composition of the myelin, although present, is altered significantly enough to impair conduction along these axons. Our previous and current data indicate that myelin composition is altered even when sheath thickness is maintained, as demonstrated by deficient MBP and PLP expression at 8 weeks despite apparently normal myelin by EM (Figure 5C; Wahl et al., 2014). A second possibility is that asynchrony of CAP conduction results in abrogation of conduction, as suggested in a previous publication (Crawford et al., 2009). Finally, perhaps the few responding myelinated axons are simply insufficient in number to elicit a measurable N1 response in the particular region we examined. Crawford and colleagues demonstrated a complete loss of N1 response using similar callosal slice recordings at 3 weeks of cuprizone demyelination, a method that does not result in a total loss of myelin even at peak demyelination. Any or all of these may be contributing to the complete loss of the N1 response even in the presence of some myelinated axons.

mTOR loss in adults using inducible *Plp-Cre^{ERT};mTOR$^{fl/fl}$* mice results in myelin deficits, indicating that mTOR is necessary for myelin maintenance. A small but significant effect on myelin thickness was observed at 12 months postinduction, with aged Plp-mTOR cKO brains exhibiting thinner myelin, particularly on smaller diameter axons. These data are strikingly similar to those observed in a study of spinal cord myelin maintenance in tamoxifen-inducible adult *Plp-Cre^{ERT}* mice lacking either or both Raptor and Rictor in MOLs (Lebrun-Julien et al., 2014). Both studies demonstrate that mTOR signaling is necessary for myelin maintenance in the CNS. However, compared with the myelin loss observed in Cnp-mTOR cKO brains, Plp-mTOR cKO brains had a milder phenotype. This may be due to a difference in recombination efficiency between the two models. While the Cnp promoter results in a recombination rate in mature OLs over 90% (Madsen et al., 2016; Wang et al., 2018), the tamoxifen paradigm used in our study recombines 60%–70% of MOLs in Plp-mTOR cKO (Jeffries et al., 2016; McLane et al., 2017). This suggests that at

least 30% of the mature OLs and myelin sheaths are likely unrecombined in the Plp-mTOR cKO brains, thereby diminishing the effect of mTOR deletion.

Cross talk between PI3K/Akt/mTOR signaling and cholesterol metabolism has been described in other cell systems (Krycer et al., 2010). In Schwann cells, as well as in other mammalian cell types, mTORC1 activates sterol regulatory element-binding proteins (SREBPs), which are master transcriptional regulators of cholesterol biosynthesis and lipogenesis (Bakan and Laplante, 2012; Eid et al., 2017; Krycer et al., 2010; Norrmen et al., 2014; Varshney and Saini, 2018). mTOR regulation of cholesterol biosynthesis in oligodendroglia may occur through similar mechanisms. While our data place mTOR upstream of cholesterol biosynthesis, studies in zebrafish additionally place mTOR downstream of cholesterol, mediating cholesterol-dependent myelin gene expression (Mathews and Appel, 2016).

Cholesterol is essential for normal myelination in the CNS (Mathews et al., 2014; Saher et al., 2005), and cells have two sources of cholesterol: *de novo* synthesis and uptake from the extracellular environment. Our data indicate that oligodendroglia are heterogeneous in their utilization of the two mechanisms for cholesterol supply. Spinal cord oligodendroglia, with higher expression of cholesterol biosynthesis enzymes, utilize *de novo* synthesis more than brain oligodendroglia. Conversely, brain oligodendroglia, with higher expression of Lrp1, likely have a greater capacity for cholesterol uptake than spinal cord oligodendroglia. Astrocyte-derived lipids are known to contribute to myelination; however, it is not known whether lipid uptake differs in brain and spinal cord oligodendrocytes (Camargo et al., 2017).

Some level of *de novo* cholesterol synthesis is still necessary in brain oligodendroglia, and when this is reduced in mTOR cKO, total cellular cholesterol is decreased. Developmentally, the brain myelinates normally in mTOR cKO animals despite lower cholesterol levels, raising the possibility that brain oligodendroglia require less cholesterol than spinal cord oligodendroglia. Axons are thicker in spinal cord white matter than in brain corpus callosum, requiring proportionally thicker myelin with longer internodes (Bray et al., 1981; Ong and Wehrli, 2010; Perge et al., 2012), and there is evidence that longer sheath length is a cell-intrinsic property of spinal cord oligodendrocytes (Bechler et al., 2015). It is noteworthy that the premyelinating oligodendroglia have transcriptomic differences between brain and spinal cord, suggesting that transcriptomic heterogeneity precedes effects of eventual structural differences after myelination is complete. Brain oligodendroglia have either a greater capacity for cholesterol uptake or a lower demand for it than oligodendroglia in the spinal cord. In either scenario, differential cholesterol synthesis provides a mechanistic basis for why mTOR loss has less impact on developmental myelination in brain than in spinal cord.

We considered the prospect of increased cholesterol availability rescuing the mTOR cKO myelin phenotype. Since cholesterol does not cross the blood-brain barrier (Bjorkhem and Meaney, 2004), oligodendroglia cannot take up dietary cholesterol, and availability is limited to cholesterol produced by neighboring cells. Thus, we were unable to attempt myelin

rescue through a high-cholesterol diet, as it would require the use of an animal model with blood-brain-barrier disruption (Saher et al., 2005, 2012).

Increased cholesterol availability promotes remyelination in mouse models of demyelinating diseases (Berghoff et al., 2017). Our data suggest that cholesterol biosynthesis through mTOR signaling has therapeutic implications in demyelinating diseases. Our findings also reveal the importance of elucidating the role of cholesterol biosynthesis in adult myelin maintenance, as this may have implications for long-term use of cholesterol-lowering drugs in humans. Indeed, there is evidence that patients taking statins, which can cross the blood-brain barrier, have lower fractional anisotropy than statin-untreated individuals, indicating deficits in white matter integrity (Ramanan et al., 2018). White matter intensities were analyzed only in patient brains and not in spinal cords; it would be interesting to investigate whether the human spinal cord has a greater myelin deficit when cholesterol levels are lowered. Further studies will be necessary to determine neurological effects of long-term statin treatment.

Limitations of the study

When investigating the divergence between brain and spinal cord precursors, we have focused on cholesterol biosynthesis because it was the most significant differentially expressed pathway. However, additional pathways, including cytoskeletal dynamics and protein kinase A signaling, are differentially expressed, and further investigation could lead to functional differences between brain and spinal cord within these pathways. We have also hypothesized, but not demonstrated, that there is greater cholesterol transfer from astrocytes to oligodendrocytes in the brain compared with the spinal cord. While we have demonstrated higher expression of Lrp1 receptor in brain oligodendroglia, astrocyte cholesterol contribution has not been analyzed. Our conclusions regarding cytoskeletal deficits of oligodendroglia in mTOR cKO cluster 7 are based on inference from RNA expression and previous literature. Identification of cluster 7 cells *in vivo* and morphological analysis would provide functional validation. Finally, we do not have a definitive explanation for the complete loss of the N1 response in callosal slice recordings due to loss of mTOR; however, a number of possible explanations are raised in the discussion.

STAR★METHODS

RESOURCE AVAILABILITY

Lead contact—Further information and requests for resources and reagents should be directed to and will be fulfilled by the lead contact, Teresa L. Wood (terri.wood@rutgers.edu).

Materials availability—Mouse lines used in this study are available upon request.

Data and code availability

- Single-cell RNA-seq data have been deposited at NCBI GEO Repository and are publicly available as of the date of publication. Accession numbers are listed in

the key resources table. Raw microscopy and western blot images reported in this paper will be shared by the lead contact upon request.

- This paper does not report original code.
- Any additional information required to reanalyze the data reported in this paper is available from the lead contact upon request.

EXPERIMENTAL MODEL DETAILS

All animal protocols were conducted in accordance with the guidelines set forth by Rutgers University and are in compliance with Institutional Animal Care and Use Committee (IACUC) guidelines and the National Institutes of Health (NIH) guidelines for the care and use of laboratory animals. All mice were bred and housed in a barrier facility with a 12-hour light/dark cycle. Mice carrying a *floxed-mTOR* allele (Carr et al., 2012; Lang et al., 2010a, 2010b) *(Mtor$^{tm1.1Clyn}$)* were provided by Dr. Christopher Lynch (Pennsylvania State College of Medicine, Hershey, PA). The *floxed-mTOR* mice were bred with a dual-reporter mouse line (B6.129(Cg)-*Gt(ROSA) 26Sortm4*$^{(ACTB-tdTomato,-EGFP)Luo}$*/J,* The Jackson Laboratory). These mice contain the *mT/mG* reporter, which globally expresses tomato red, and, in cells with active Cre-recombinase, express GFP. *CNP-Cre* mice (Lappe-Siefke et al., 2003) were obtained from K. Nave. All strains were on a C57/Bl/6 background. Mice homozygous for *mTOR floxed* and *mT/mG* reporter alleles and heterozygous for *CNP-Cre* were used for breeding to generate Cre+ or Cre− littermates for experiments. The resultant *mTOR$^{fl/fl}$* mice expressing Cre (*Cre*+/−) have been previously described (Wahl et al., 2014) and are hereafter referred to as mTOR cKO with *mTOR$^{fl/fl}$/Cre−/−* littermates used as controls. Both males and females were used in all analyses. For all experiments P0 designated the day of birth.

METHOD DETAILS

Isolation of O4+ cells and efficiency analysis—Control (Cre−/−) and mTOR cKO littermates were used at P14 for O4+ cell isolation from brains and at P10 for isolation from spinal cord (Figure S1C). Mice were rapidly decapitated and spinal cords or brains were dissected. Brain dissection at P14 included forebrain and midbrain, and excluded olfactory bulb, cerebellum, and brainstem. Spinal cord dissection at P10 included whole spinal cord. Tissues were dissociated into single cells using Neural Dissociation Kit (P) (Miltenyi). The proportion of cells in the P10 spinal cord and P14 brain that had matured to an O4+ stage was analyzed by flow cytometry (Figures S1A and S1B). Cells were incubated with FcR blocking reagent and then stained with O4-APC antibody (1:10, Miltenyi) by incubating for 10 min at 4°C. Cells were then washed twice in PBS with 0.5% BSA and 2 mM EDTA and run on LSR II flow cytometer (BD Biosciences).

For isolation of O4+ oligodendroglia, dissociated cells from control mice were pooled together and mTOR cKO mice were pooled together. O4+ oligodendroglia were isolated by magnetic-activated cell sorting using anti-O4 microbeads (Miltenyi) and eluted into PBS with 0.5% BSA. Isolation efficiency was analyzed by flow cytometry of the negative and positive isolation fractions (Figure S1D) by staining with O4-APC antibody as described above. Data were analyzed using FlowJo software. Isolation efficiency was determined to be ~90% by flow cytometry (Figure S1D), and mRNA expression of oligodendrocyte-specific

genes was consistent with previously reported characterization of O4+ cells (Lin et al., 2009).

Primary rat OPC cultures—OPCs were purified from cortical mixed glial cultures by established methods (McCarthy and de Vellis, 1980). Brains were removed from postnatal day 0–2 Sprague Dawley rat pups and the cortices were dissected. Cortical pieces were enzymatically digested in 2.5% trypsin and Dnase I followed by mechanical dissociation. Cells were resuspended in MEM-C, which consisted of minimal essential media (MEM) supplemented with 10% FBS, L-glutamine, and 1% Pen-strep, and plated in T75 flasks. The resulting mixed glial cultures were maintained until confluent for a day (~10 days total). Purified OPC cultures were prepared by a differential shake. Purified OPCs were seeded onto poly-D-lysine coated T75 flasks at a density of 1.5×10^4 cells/cm2 in N2S media. N2S consists of 66% N2B2 (DMEM/F12 supplemented with 0.66 mg/ml BSA, 10 ng/ml d-biotin, 5 μg/ml insulin, 20 nM progesterone, 100 μM putrescine, 5 ng/ml selenium, 50 μg/ml apo-transferrin, 100 U/ml penicillin, 100 μg/ml streptomycin, and 0.5% FBS) supplemented with 34% B104 conditioned media, 5 ng/ml FGF, and 0.5% FBS. To initiate oligodendrocyte differentiation, we followed an established mitogen withdrawal protocol (Tokumoto et al., 1999). After overnight recovery in N2S, media was replaced with Differentiation media (mitogen free N2B2 media supplemented with 30 ng/ml triiodothyronine (T3)). Differentiation media with or without inhibitors was replenished every 48 hr over the course of experiments. Cell culture media (MEM, DMEM/F12), FBS, trypsin, and insulin-selenium-transferrin (ITS) were purchased from Gibco (Long Island, NY). Additional N2 supplements, T3, and poly-d-lysine were purchased from Sigma. Recombinant human FGF-2 was purchased from R&D Systems (Minneapolis, MN).

Treatment with inhibitors—To inhibit mTOR, cells were treated with 10 nM rapamycin (Calbiochem, 553210) which is an effective dose based on our prior studies (Tyler et al., 2009, 2011). Stock solutions of 5 mM rapamycin were prepared in DMSO. Control cultures received vehicle alone.

To inhibit cholesterol biosynthesis, cells were treated with simvastatin (Millipore, 567022). Stock solutions of 1 mM simvastatin were prepared in DMSO. While the effective dose of simvastatin for HMGCR inhibition in oligodendroglia *in vitro* is unclear, the IC_{80} for cholesterol synthesis in rat hepatocytes is approximately 5 μM simvastatin(Masters et al., 1995). Therefore, we treated differentiating primary rat OPCs with 5 μM and 1 μM simvastatin. Control cultures received vehicle alone.

Protein extraction and immunoblotting—For analyses at P10, P14, and P18, O4 cells were isolated and lysed in RIPA lysis buffer (Thermo Scientific, 89900) with 1× Halt Protease/Phosphatase Inhibitor Cocktail (Thermo Scientific, 78440). For analyses at 8 weeks and 12 weeks, brains were dissected from control and mTOR cKO mice. Brains were cut into 2 mm wide coronal slices directly above the hippocampus using a brain mold. The midline corpus callosum was microdissected from the coronal slice and immediately frozen in Eppendorf tubes on dry ice. To prepare protein samples, frozen samples were ground into a fine powder using a micro-mortar and pestle. Samples were then lysed using 60 μL RIPA

buffer with 1× Halt Protease/Phosphatase Inhibitor Cocktail. Samples were gently pipetted for 1 min to homogenize.

The RC-DC protein assay (BioRad) was performed to determine protein concentration. 20 μg of protein was resolved by SDS-PAGE on 4–12% Bis-Tris mini-gels (Invitrogen). Separated proteins were transferred to nitrocellulose membranes and blocked in 5% milk/TBS-0.1% Tween for 2 hr at room temperature. Membranes were then incubated in the presence of primary antibodies diluted in 5% BSA/TBS-0.1% Tween overnight at 4°C. The exception was anti-FDPS which was incubated in 5% milk/TBS-0.1% Tween for 1.5 hr at room temperature. Membranes were then washed 3 times for 10 min with TBS-0.1% Tween and incubated for 1 hr at room temperature in 5% milk/TBS-0.1% Tween containing goat anti-rabbit or goat anti-mouse HRP-conjugated secondary antibodies at a dilution of 1:5000. The detection of HRP conjugated secondary antibodies was performed by enhanced chemiluminescence using the Ultra-LUM imaging device. Protein expression levels were quantified using Image J. The following antibodies were used: Hmgcr (Invitrogen, PA5-37367 1:500), Hmgcs1 (Cell Signaling, 42201S, 1:1000), Fdps (Proteintech, 16129-1-AP, 1:1000), Lrp1 (Abcam, ab92544 1:12,000), β-actin (Sigma, A5441, 1:5000), MBP (Covance, SMI-99, 1:500), PLP (Clone AA3, gift from the Macklin Lab, 1:40000), β-tubulin (Cell Signaling, 5346S, 1:1000), and β-amyloid (Invitrogen, 51–2700, 1:1000), SMI-32 (Biolegend, 801701, 1:500). Statistical analysis was performed using GraphPad Prism. Unpaired two-tailed t test was performed to determine significance.

Quantitative real-time PCR—RNA was extracted using RNeasy Plus Mini Kit (Qiagen, Valencia, CA). RNA concentration was measured using a NanoDrop spectrophotometer (Thermo Scientific) and cDNA was reverse transcribed using Superscript II (Invitrogen). RT-PCR was performed using SYBR green detection master mix (BioRad 430001607) and amplification was normalized to expression levels of Gapdh for each sample. β-actin was used as an additional housekeeping control to confirm that Gapdh expression was constant in treated oligodendroglia in all conditions. RT-PCR was performed on the Applied Biosystems 7900B (Carlsbad, CA) using the associated Sequence Detection System Version 2.2.2. The thermal reaction profiles for the PCRs were performed as follows: 50°C for 2 min, 9°C for 10 min, 40 cycles of 95°C for 15 s, and 58°C for 1 min. BioRad plates and QuantiTect primers were used. Primers (Qiagen): Gapdh QT00199633, Mbp QT00199255, Mag QT00195391, Plp1 QT00176414, Hmgcr QT00182861, Hmgcs1 QT00183267, Fdps QT00175574, β-actin QT00193473. Statistical analysis for each target was performed using unpaired two-tailed t test (Figure 5C) or one-way ANOVA followed by Tukey's post hoc multiple comparisons test (Figure 6) in GraphPad Prism.

Cholesterol analysis—Brain and spinal cord tissue were dissected from mice at P14 and P10, respectively and O4+ cells were isolated as described above. Neutral lipids were extracted using a modified Folch method (Folch et al., 1957). Cells were homogenized in ice-cold chloroform:methanol (2:1) and incubated at room temperature for 2 hours. Following addition of 0.2 volumes 0.9% sodium chloride, each sample was centrifuged at 2000×g, 4°C for 10 minutes. The organic phase was removed, dehydrated overnight, and resuspended in a butanol:Triton-X:methanol solution (0.6/0.267/0.133). Cholesterol content

was determined using an enzymatic colorimetric cholesterol assay (StanBio Laboratory, Boerne, TX) and normalized to cell count. Unpaired two-tailed t test was performed to determine significance using GraphPad Prism.

Cell viability assay—Cell viability was measured after 3 days and 5 days of culture using an MTT [3-(4,5-dimethyldiazol-2-yl)-2,5-diphenyl tetrazolium bromide] assay (Abcam, ab211091) as per manufacturer's protocol. Briefly, cells were incubated with MTT reagent for 3 hours at 37°C before adding MTT solvent and mixing on an orbital shaker for 15 mins. Absorbance was measured at OD590 nm and results were normalized to control culture conditions. Each condition was plated and analyzed in triplicate and the experiment was repeated three times. Statistical analysis for was performed using one-way ANOVA followed by Tukey's post hoc multiple comparisons test in GraphPad Prism.

Tissue preparation and immunostaining—mTOR cKO animals and corresponding controls were taken for analysis at 7–8 weeks and 12 weeks of age. A total of four to six animals per genotype from the corresponding time point were used for all analyses described. Mice were intracardially perfused with 10 mL of an ice-cold PBS solution containing phosphatase inhibitors and heparin followed by 40 mL of ice-cold 3% paraformaldehyde (PFA) at a rate of 2 mL/min. Brains were dissected and cut into 2 mm wide coronal slices directly above the hippocampus using a brain mold and drop-fixed in 3% PFA overnight. The tissue was then dehydrated with a 30% sucrose solution and subsequently frozen in OCT. 20 μm serial sections were taken throughout the brain slices. Immunolabeling was performed as described previously (McLane et al., 2017), with specific treatments used for antibody staining as necessary. Mounted cryosections were rinsed in TBS. For myelin oligodendrocyte glycoprotein (MOG) staining, sections were delipidated for 10 min in 100% ethanol then treated with 3% hydrogen peroxide to eliminate endogenous peroxidase activity. For SOX10 and cleaved caspase-3 staining, sections were soaked for 10 min in 0.01 M sodium citrate buffer heated to boiling before immersion. All sections were permeabilized in 1% Triton X-100 and 2% normal serum for 30 min, and then blocked in a solution containing 10% BSA and 10% normal serum for 1 h. Normal serum was from goat or donkey, depending on the species in which the secondary antibody was raised. Primary antibodies were incubated at 4°C overnight. Sections were washed in TBS with 0.05% Triton X-100 and incubated in secondary antibodies for 2 h. Both primary and secondary antibodies were diluted in a TBS solution containing 2% BSA, 2% serum, and 0.2% Triton X-100. For MOG staining, The NovaRed substrate kit (SK-4800, Vector Laboratories) was used to detect positive signal, then slides were dehydrated in ethanol and coverslipped with Cytoseal (8312–4, Thermo Scientific). Primary antibodies used: goat anti-SOX10 (1:50, AF2864, R&D Systems), rabbit anti-cleaved caspase-3 (1:400, 9664S, Cell Signaling), rabbit anti-MOG (1:1000, ab32760, Abcam), mouse anti-CASPR (1:200, MABN69, Millipore), and rabbit anti-NaV1.6 (1:300, ASC-009, Alomone Labs). Secondary antibodies used: donkey anti-mouse 647 (1:500, A31571, Life Technologies), donkey anti-goat AMCA (1:100, 705-155-147, Jackson Laboratories), donkey anti-rabbit 647 (1:750, A31573, Life Technologies), goat anti-mouse 647 (1:500, A21235, Life Technologies), and biotinylated goat anti-rabbit (1:500, BA-1000, Vector Laboratories) followed by streptavidin-HRP (1:1000, 21126, Pierce). Immunofluorescent stained sections

were coverslipped using Fluorogel (17985–10, Electron Microscopy Sciences) then sealed with nail lacquer.

MOG image analysis—To analyze MOG immunostaining, images were taken with a 2× objective using an Olympus AX-70 microscope and analyses were performed using ImageJ software. The entire midline callosum visible in each 2× image was outlined as the ROI. MOG positivity was defined using the adjust threshold function for positive staining and the area fraction within the ROI was calculated using ImageJ software. Data were then expressed as a percentage of the total ROI. At least 3–4 images/animal and 3–8 animals/group were analyzed. Unpaired two-tailed t test was performed to determine significance using GraphPad Prism.

Cell counts—To analyze SOX10/cleaved caspase-3 immunostaining, images were taken with a 20× objective using an Olympus AX-70 microscope. Cell counts were performed using ImageJ software with the cell counter plugin. The midline callosum visible within the image was outlined as the ROI. The area in μm^2 for each ROI was used to normalize all data to mm^2. For all counts, 3–4 images/animal and 6 animals/group were analyzed. All SOX10+ cells within an ROI were counted, followed by all double-immunolabeled cleaved caspase-3+/SOX10+ cells. To analyze CASPR and NaV1.6 immunostaining, images were taken with a 60× oil objective using an A1R confocal microscope. Counts of nodal structures, defined as two CASPR+ paranodes on either side of a NaV1.6+ node, were performed using ImageJ software and the cell counter plugin. The entire image (2621.44 μm^2) was used as the ROI. For all counts, 3–4 images/animal and 3 animals/group were analyzed. Unpaired two-tailed t test was performed to determine significance using GraphPad Prism.

Electron microscopy—Mice were perfused and brains were dissected as described above. A 2 mm region just rostral of the hippocampus was drop-fixed in 2% PFA/2.5% glutaraldehyde (01909–100, Polysciences, Inc.) at 4°C overnight. Using a PELCO Biowave Pro tissue processor (Ted Pella), the tissue was rinsed in 100 mM cacodylate buffer and then post-fixed in a reduced osmium mixture consisting of 1% osmium tetroxide and 1.5% potassium ferrocyanide followed by 1% osmium tetroxide alone. Dehydration was carried out in a graded series of acetone (50%, 70%, 90%, 100%) containing 2% uranyl acetate for *en bloc* staining. Finally, tissue was infiltrated and embedded in Embed 812 (Electron Microscopy Services) and cured for 48 hr at 60°C in an oven. The corpus callosum pieces were oriented such that sections could be cut midline in a sagittal plane. Ultrathin sections (65 nm) were mounted on copper mesh grids and viewed at 80 kV on a Tecnai G2 transmission electron microscope (FEI). Electron micrographs of the corpus callosum were imaged near the midline.

In order to calculate g-ratios, all axons within 3 electron micrographs/animal were measured using ImageJ software to calculate the area of each axon as well as the total area of the myelinated fiber. Axon diameter and total myelinated fiber diameter were then extracted from each measured area in Microsoft Excel. At least 199 and up to 565 axons were measured in each animal with 3 animals/group. G-ratio was calculated as axon diameter/total myelinated fiber diameter. For scatter plots and g-ratio distribution graphs, all measured

g-ratios were plotted. In order to examine number of myelinated axons, all myelinated axons within 3 electron micrographs/animal were counted using ImageJ software and the cell counter plugin. The number of myelinated axons within each animal was defined as the average number of myelinated axons in each micrograph. The ROI was defined as the entire micrograph area, 141.23 μm^2. For g-ratio scatter plots, linear regression analyses were used to compare the slope and y-intercept of the control and Cnp-mTOR cKO or Plp-mTOR cKO linear regressions using all measured g-ratios. For g-ratio distribution analysis, the Kolmogirov-Smirnov t-test was used in order to compare cumulative ranks using all measured g-ratios.

Callosal slice electrophysiology—Electrophysiology recordings were performed *in vitro* on coronal slices of control and mTOR cKO brains. Slicing ACSF (125 mM NaCl, 2.4 mM KCl, 2 mM MgCl2, 1.015 mM NaH2PO4.H2O, 26.40 mM NaHCO3, 2.04 mM CaCl2.2H2O, and 11 mM Glucose) and recording ACSF (125 mM NaCl, 2.4 mM KCl, 1.4 mM MgCl2, 1.015 mM NaH2PO4, 26.40 mM NaHCO3, 2.18 mM CaCl2.2H2O, and 24.94 mM Glucose) were prepared. Mice were anesthetized using isoflurane and quickly decapitated. Brains were rapidly dissected and submerged in ice-cold slicing ACSF solution for 3 min. The cerebellum and 1/3 of prefrontal/frontal cortex were separated and the rest of the brain was submerged in the same solution for an additional 3 min. After the brains were adequately cooled, coronal slices of 400 μm thickness were prepared using a LEICA VT 1200S vibratome. The coronal slices were incubated in oxygenated half slicing–half recording ACSF solution (to prevent glucose shock) for 2 hours at 31–32°C. Electrophysiology recordings were done on the corpus callosum. The FHC concentric bipolar stimulation electrode, CBBPE75, was inserted on one hemisphere and the micropipette glass recording electrode filled with 3M NaCl was located on the other hemisphere (Figure S9G). The Axon Digidata 1550B and Multiclamp 700B of Molecular Devices were used to acquire and amplify the extracellular signal. Field compound action potentials (CAP) recorded through the recording electrode were analyzed for N1 (myelinated fiber) as well as N2 (unmyelinated fiber) amplitude, latency, and duration. For slice recording analyses, Student's t-test was performed using all measured recordings from control and Cnp-mTOR cKO groups. All data are presented as mean ± SEM.

QUANTIFICATION AND STATISTICAL ANALYSIS

Single-cell sequencing—We utilized 10× Genomics platform for single-cell RNA-Seq (Figure S1C). Droplet-based single-cell partitioning and single-cell RNA-Seq libraries were generated using the 10X Chromium Controller and the Chromium Single-Cell 3′ Reagent v3 Kit (10X Genomics, Pleasanton, CA) as per the manufacturer's protocol. Live O4+ cells in single cell suspension at a concentration of 600 cells/μL were mixed with RT reagents and loaded onto a Single-Cell 3′ Chip along with Gel beads and Partitioning oil in the recommended order and then the chip was processed through 10X Chromium Controller for the generation of Gel Beads-in-Emulsion (GEMs). GEM generation was followed by 3′ Gene Expression Library prep protocol that includes Reverse Transcription, cleanup, cDNA amplification, fragmentation, end repair & A-tail prep, adapter ligation and incorporation of i7sample indices into finished libraries, which are compatible with Illumina next-generation sequencing platforms. Sample quantification and quality control

were determined using Qubit Fluorometer (Invitrogen, Life Technologies) and TapeStation (Agilent Technologies, Santa Clara CA) respectively. The cDNA libraries were sequenced on Illumina NextSeq500 sequencer (Illumina, San Diego, CA) with a configuration of 26/8/0/98 cycles (Read1–10XBarcode+UMI/i7index/i5index/ Read2- mRNA reads). Single-cell sequencing was done at the Genomics Center, Rutgers New Jersey Medical School and sequencing on the NextSeq 500 was supported by National Institutes of Health grant (S10 OD018206).

Sequencing data pre-processing and quality control—The cellranger mkfastq pipeline (Cell Ranger Version 3.0.2) was used to process the sequencing run generated as described above, and single-cell gene expression was quantified using cellranger count pipeline (Cell Ranger Version 3.0.2). Subsequent QC and analysis were performed using Seurat package version 3.0.2 within R 3.6.0. Cells with mitochondrial gene counts greater than 5% were removed. To minimize potential ambient RNA or duplets/multiplets, cells with transcript numbers between 500 and 3000 were selected for downstream analysis. Contaminating non-oligodendroglial cells were eliminated when highly expressing the following gene markers: *Hbb-bs* (erythrocytes), *Aif1, CD68* (microglia), *Ptprc* (leukocytes), *Gfap, Slc1a3* (astrocytes), *Rbfox3* (neurons), *Pecam1* (endothelial cells), *Ttr* (choroid plexus epithelial cells). After filtering, a total of 9325 cells from spinal cord (3879 control cells, 5446 mTOR cKO cells) were obtained, and a total of 16397 cells from brain (8220 control cells, 8177 mTOR cKO cells) were obtained.

Data normalization, clustering, and integration—Data were normalized using the default scaling factor of 10000. Principal component analysis was performed prior to clustering and the first 17 principal components (PCs) were used based on the ElbowPlot. Unsupervised clustering was performed using the FindClusters function with a resolution of 0.5. The non-linear dimensional reduction and Uniform Manifold Approximation and Projection (UMAP) analysis were performed using the same PCs used in the clustering analysis. With 2 dimensional reductions, both PCA analysis and UMAP calculated, the samples were integrated together using a computational strategy described by Stuart, T. et al. (Stuart et al., 2019). Some non-oligodendroglial cells survived the pre-processing and clustered together after integration. These were further identified using marker genes listed above and were removed, resulting in the final dataset of 4603 brain control cells, 3887 brain mTOR cKO cells, 3605 spinal cord control cells, 5233 spinal cord mTOR cKO cells, which were re-integrated and re-clustered for the downstream analysis. Control brain and control spinal cord O4+ cells were integrated together to analyze regional heterogeneity on one UMAP plot, and all four samples (control brain and spinal cord, mTOR cKO brain and spinal cord) were plotted integrated on a second UMAP plot to analyze effects of mTOR loss.

Analysis of differential gene expression—Following unsupervised clustering, cell types were determined for each cluster using marker genes and published databases (Zhang et al., 2014; Marques et al., 2016). Differential expression of genes between conditions or clusters was performed using the Find-Marker function of the Seurat package, which identifies negative and positive markers for each condition or cluster. A gene is required

to be detected at a minimum 20–25% in either of the two groups of cells. All genes demonstrating statistically significant differential expression were included in downstream analyses. The top 5 differentially expressed genes in each cluster (when compared to all others) were used to identify cellular identity and differentiation stage of the cluster (Figures S2B and S5C). Genes were searched in the Barres database (Zhang et al., 2014) and Castelo-Branco single-cell database (Marques et al., 2016) and results are shown in Figures S2C and S5D.

Differential gene expression data were further analyzed using IPA (QIAGEN, https://www.qiagenbioinformatics.com/products/ingenuity-pathway-analysis). Network analysis in Figure S3A was generated using IPA.

Analysis of frequency and proportion equality—For integrated sample analysis, the number of cells in each cluster was examined and percentage of cell source sample in different clusters was analyzed using two-proportions z-test for equality of proportions. A classical P value was calculated to evaluate the statistical significance.

Analysis of trajectory and pseudotime—The monocle3 version 0.2.1 within R 3.6.3 was used for trajectory and pseudotime analysis. Cells from the 4 samples integrated in Seurat were used to construct the monocle plot. Seurat clustering information was preserved to facilitate the interpretation of the pseudotime analysis. Cells were ordered according to its progress along a learned trajectory, which is termed as “pseudotime” in monocle. Clusters 8 and 7 were identified as OPCs (Figure S2) which are the least differentiated clusters and were therefore selected as the root group for pseudotime analysis.

Other statistical analysis—Data and were analyzed and statistical significance determined using GraphPad Prism version 8.3.0. Datasets with one variable (treatment) and two groups were analyzed by Student’s t test. P values of <0.05 were considered significant. *$p < 0.05$, **$p < 0.01$, ***$p < 0.001$, ****$p < 0.0001$. Data are presented as mean ± standard error of the mean (SEM) or mean ± standard deviation (SD). For single-cell clusters, the percentage of cell source sample in different clusters was analyzed using two-proportions z-test for equality of proportions. For g-ratio scatter plots, linear regression analyses were used to determine statistical significance. For g-ratio distribution analysis, the Kolmogirov-Smirnov t-test was used in order to compare cumulative ranks using all measured g-ratios. The number of replicate samples or animals analyzed in each experiment is indicated in the figures legends as n= value.

Supplementary Material

Refer to Web version on PubMed Central for supplementary material.

ACKNOWLEDGMENTS

We thank Alex Lemenze and Robert Donnelly for initial assistance with single-cell transcriptomics, Quan Shang for technical assistance, and Andrew Thomas for helpful discussions. We also thank Mainul Hoque and Neeraja Syed at the Rutgers NJMS Genomics Center for sequencing performed on Illumina NextSeq 500 (NIH SIG grant 1S10OD018206-01A1). The authors acknowledge the Office of Advanced Research Computing (OARC) at Rutgers, The State University of New Jersey, for providing access to the Amarel cluster and associated research

computing resources that have contributed to the results reported here (URL: https://oarc.rutgers.edu). This work was supported by National Institute of Neurological Disorders and Stroke R01/R37 NS082203 to T.L.W. and W.B.M., F31 NS108521 to M.A.J., and National Multiple Sclerosis Society RG5371-A-4 to T.L.W.

REFERENCES

Bakan I, and Laplante M (2012). Connecting mTORC1 signaling to SREBP-1 activation. Curr. Opin. Lipidol 23, 226–234. 10.1097/MOL.0b013e328352dd03. [PubMed: 22449814]

Bechler ME, Byrne L, and Ffrench-Constant C (2015). CNS myelin sheath lengths are an intrinsic property of oligodendrocytes. Curr. Biol 25, 2411–2416. 10.1016/j.cub.2015.07.056. [PubMed: 26320951]

Benardais IMO, Fauveau M, Brown TL, Lisbet T, Finseth LT, Panic R, Deboux C, Macklin WB, Wood TL, and Oumesmar BN (2022). p70S6 kinase regulates oligodendrocyte differentiation and is active in remyelinating lesions. Brain Commun.

Bercury KK, Dai J, Sachs HH, Ahrendsen JT, Wood TL, and Macklin WB (2014). Conditional ablation of raptor or rictor has differential impact on oligodendrocyte differentiation and CNS myelination. J. Neurosci 34, 4466–4480. 10.1523/JNEUROSCI.4314-13.2014. [PubMed: 24671993]

Berghoff SA, Gerndt N, Winchenbach J, Stumpf SK, Hosang L, Odoardi F, Ruhwedel T, Bohler C, Barrette B, Stassart R, et al. (2017). Dietary cholesterol promotes repair of demyelinated lesions in the adult brain. Nat. Commun 8, 14241. 10.1038/ncomms14241. [PubMed: 28117328]

Bjorkhem I, and Meaney S (2004). Brain cholesterol: long secret life behind a barrier. Arterioscler Thromb. Vasc. Biol 24, 806–815. 10.1161/01.ATV.0000120374.59826.1b. [PubMed: 14764421]

Bray GM, Rasminsky M, and Aguayo AJ (1981). Interactions between axons and their sheath cells. Annu. Rev. Neurosci 4, 127–162. 10.1146/annurev.ne.04.030181.001015. [PubMed: 7013633]

Brown TL, Hashimoto H, Finseth LT, Wood TL, and Macklin WB (2021). PAK1 positively regulates oligodendrocyte morphology and myelination. J. Neurosci 41, 1864–1877. 10.1523/JNEUROSCI.0229-20.2021. [PubMed: 33478987]

Brown TL, and Macklin WB (2020). The actin cytoskeleton in myelinating cells. Neurochem. Res 45, 684–693. 10.1007/s11064-019-02753-0. [PubMed: 30847860]

Camargo N, Goudriaan A, van Deijk AF, Otte WM, Brouwers JF, Lodder H, Gutmann DH, Nave KA, Dijkhuizen RM, Mansvelder HD, et al. (2017). Oligodendroglial myelination requires astrocyte-derived lipids. PLoS Biol 15, e1002605. [PubMed: 28549068]

Carr TD, DiGiovanni J, Lynch CJ, and Shantz LM (2012). Inhibition of mTOR suppresses UVB-induced keratinocyte proliferation and survival. Cancer Prev. Res. (Phila) 5, 1394–1404. 10.1158/1940-6207.CAPR-12-0272-T. [PubMed: 23129577]

Crawford AH, Tripathi RB, Richardson WD, and Franklin RJM (2016). Developmental origin of oligodendrocyte lineage cells determines response to demyelination and susceptibility to age-associated functional decline. Cell Rep. 15, 761–773. 10.1016/j.celrep.2016.03.069. [PubMed: 27149850]

Crawford DK, Mangiardi M, Xia X, Lopez-Valdes HE, and Tiwari-Woodruff SK (2009). Functional recovery of callosal axons following demyelination: a critical window. Neuroscience 164, 1407–1421. [PubMed: 19800949]

Del Rio-Hortega P (2012). Studies on neuroglia: glia with very few processes (oligodendroglia) by PA-o del RA-o-Hortega. 1921. Clin. Neuropathol 31, 440–459. 10.5414/NP300999. [PubMed: 23083463]

Domingues HS, Cruz A, Chan JR, Relvas JB, Rubinstein B, and Pinto IM (2018). Mechanical plasticity during oligodendrocyte differentiation and myelination. Glia 66, 5–14. 10.1002/glia.23206. [PubMed: 28940651]

Eid W, Dauner K, Courtney KC, Gagnon A, Parks RJ, Sorisky A, and Zha X (2017). mTORC1 activates SREBP-2 by suppressing cholesterol trafficking to lysosomes in mammalian cells. Proc. Natl. Acad. Sci. U S A 114, 7999–8004. 10.1073/pnas.1705304114. [PubMed: 28696297]

de los Monteros AE, Kumar S, Zhao P, Huang CJ, Nazarian R, Pan T, Scully S, Chang R, and de Vellis J (1999). Transferrin is an essential factor for myelination. Neurochem. Res 24, 235–248. 10.1007/s11064-004-1826-2. [PubMed: 9972870]

Folch J, Lees M, and Sloane Stanley GH (1957). A simple method for the isolation and purification of total lipides from animal tissues. J. Biol. Chem 226, 497–509. [PubMed: 13428781]

Foran DR, and Peterson AC (1992). Myelin acquisition in the central nervous system of the mouse revealed by an MBP-Lac Z transgene. J. Neurosci 12, 4890–4897. [PubMed: 1281497]

Hammelrath L, Skokic S, Khmelinskii A, Hess A, van der Knaap N, Staring M, Lelieveldt BPF, Wiedermann D, and Hoehn M (2016). Morphological maturation of the mouse brain: an in vivo MRI and histology investigation. Neuroimage 125, 144–152. 10.1016/j.neuroimage.2015.10.009. [PubMed: 26458518]

Jeffries MA, Urbanek K, Torres L, Wendell SG, Rubio ME, and Fyffe-Maricich SL (2016). ERK1/2 activation in preexisting oligodendrocytes of adult mice drives new myelin synthesis and enhanced CNS function. J. Neurosci 36, 9186–9200. 10.1523/JNEUROSCI.1444-16.2016. [PubMed: 27581459]

Klein C, Kramer EM, Cardine AM, Schraven B, Brandt R, and Trotter J (2002). Process outgrowth of oligodendrocytes is promoted by interaction of fyn kinase with the cytoskeletal protein tau. J. Neurosci 22, 698–707. [PubMed: 11826099]

Krycer JR, Sharpe LJ, Luu W, and Brown AJ (2010). The Akt-SREBP nexus: cell signaling meets lipid metabolism. Trends Endocrinol. Metab 21, 268–276. 10.1016/j.tem.2010.01.001. [PubMed: 20117946]

Lang CH, Lynch CJ, and Vary TC (2010a). Alcohol-induced IGF-I resistance is ameliorated in mice deficient for mitochondrial branched-chain aminotransferase. J. Nutr 140, 932–938. 10.3945/jn.109.120501. [PubMed: 20237068]

Lang SA, Hackl C, Moser C, Fichtner-Feigl S, Koehl GE, Schlitt HJ, Geissler EK, and Stoeltzing O (2010b). Implication of RICTOR in the mTOR inhibitor-mediated induction of insulin-like growth factor-I receptor (IGF-IR) and human epidermal growth factor receptor-2 (Her2) expression in gastrointestinal cancer cells. Biochim. Biophys. Acta 1803, 435–442. 10.1016/j.bbamcr.2010.01.009. [PubMed: 20116405]

Lappe-Siefke C, Goebbels S, Gravel M, Nicksch E, Lee J, Braun PE, Griffiths IR, and Nave KA (2003). Disruption of Cnp1 uncouples oligodendroglial functions in axonal support and myelination. Nat. Genet 33, 366–374. 10.1038/ng1095. [PubMed: 12590258]

Lebrun-Julien F, Bachmann L, Norrmen C, Trotzmuller M, Kofeler H, Ruegg MA, Hall MN, and Suter U (2014). Balanced mTORC1 activity in oligodendrocytes is required for accurate CNS myelination. J. Neurosci 34, 8432–8448. 10.1523/JNEUROSCI.1105-14.2014. [PubMed: 24948799]

Lin G, Mela A, Guilfoyle EM, and Goldman JE (2009). Neonatal and adult O4(+) oligodendrocyte lineage cells display different growth factor responses and different gene expression patterns. J. Neurosci. Res 87, 3390–3402. 10.1002/jnr.22065. [PubMed: 19360905]

Lin JP, Mironova YA, Shrager P, and Giger RJ (2017). LRP1 regulates peroxisome biogenesis and cholesterol homeostasis in oligodendrocytes and is required for proper CNS myelin development and repair. Elife 6. 10.7554/eLife.30498.

Liu A, Muggironi M, Marin-Husstege M, and Casaccia-Bonnefil P (2003). Oligodendrocyte process outgrowth in vitro is modulated by epigenetic regulation of cytoskeletal severing proteins. Glia 44, 264–274. 10.1002/glia.10290. [PubMed: 14603467]

Madsen PM, Motti D, Karmally S, Szymkowski DE, Lambertsen KL, Bethea JR, and Brambilla R (2016). Oligodendroglial TNFR2 mediates membrane TNF-dependent repair in experimental autoimmune encephalomyelitis by promoting oligodendrocyte differentiation and remyelination. J. Neurosci 36, 5128–5143. 10.1523/JNEUROSCI.0211-16.2016. [PubMed: 27147664]

Mahley RW (1988). Apolipoprotein E: cholesterol transport protein with expanding role in cell biology. Science 240, 622–630. 10.1126/science.3283935. [PubMed: 3283935]

Marisca R, Hoche T, Agirre E, Hoodless LJ, Barkey W, Auer F, Castelo-Branco G, and Czopka T (2020). Functionally distinct subgroups of oligodendrocyte precursor cells integrate neural activity and execute myelin formation. Nat. Neurosci 23, 363–374. 10.1038/s41593-019-0581-2. [PubMed: 32066987]

Marques S, van Bruggen D, Vanichkina DP, Floriddia EM, Munguba H, Varemo L, Giacomello S, Falcao AM, Meijer M, Bjorklund AK, et al. (2018). Transcriptional convergence of

oligodendrocyte lineage progenitors during development. Dev. Cell 46, 504–517.e7. 10.1016/j.devcel.2018.07.005. [PubMed: 30078729]

Marques S, Zeisel A, Codeluppi S, van Bruggen D, Mendanha Falcao A, Xiao L, Li H, Haring M, Hochgerner H, Romanov RA, et al. (2016). Oligodendrocyte heterogeneity in the mouse juvenile and adult central nervous system. Science 352, 1326–1329. 10.1126/science.aaf6463. [PubMed: 27284195]

Masters BA, Palmoski MJ, Flint OP, Gregg RE, Wang-Iverson D, and Durham SK (1995). In vitro myotoxicity of the 3-hydroxy-3-methylglutaryl coenzyme A reductase inhibitors, pravastatin, lovastatin, and simvastatin, using neonatal rat skeletal myocytes. Toxicol. Appl. Pharmacol 131, 163–174. 10.1006/taap.1995.1058. [PubMed: 7878672]

Mathews ES, and Appel B (2016). Cholesterol Biosynthesis Supports Myelin Gene Expression and Axon Ensheathment through Modulation of P13K/Akt/mTor Signaling. J Neurosci 36, 7628–7639. [PubMed: 27445141]

Mathews ES, Mawdsley DJ, Walker M, Hines JH, Pozzoli M, and Appel B (2014). Mutation of 3-hydroxy-3-methylglutaryl CoA synthase I reveals requirements for isoprenoid and cholesterol synthesis in oligodendrocyte migration arrest, axon wrapping, and myelin gene expression. J. Neurosci 34, 3402–3412. 10.1523/JNEUROSCI.4587-13.2014. [PubMed: 24573296]

McCarthy KD, and de Vellis J (1980). Preparation of separate astroglial and oligodendroglial cell cultures from rat cerebral tissue. J. Cell Biol 85, 890–902. 10.1083/jcb.85.3.890. [PubMed: 6248568]

McLane LE, Bourne JN, Evangelou AV, Khandker L, Macklin WB, and Wood TL (2017). Loss of tuberous sclerosis Complex1 in adult oligodendrocyte progenitor cells enhances axon remyelination and increases myelin thickness after a focal demyelination. J. Neurosci 37, 7534–7546. 10.1523/JNEUROSCI.3454-16.2017. [PubMed: 28694334]

Miron VE, Zehntner SP, Kuhlmann T, Ludwin SK, Owens T, Kennedy TE, Bedell BJ, and Antel JP (2009). Statin therapy inhibits remyelination in the central nervous system. Am. J. Pathol 174, 1880–1890. 10.2353/ajpath.2009.080947. [PubMed: 19349355]

Musah AS, Brown TL, Jeffries MA, Shang Q, Hashimoto H, Evangelou AV, Kowalski A, Batish M, Macklin WB, and Wood TL (2020). Mechanistic target of rapamycin regulates the oligodendrocyte cytoskeleton during myelination. J. Neurosci 40, 2993–3007. 10.1523/JNEUROSCI.1434-18.2020. [PubMed: 32139584]

Nawaz S, Sanchez P, Schmitt S, Snaidero N, Mitkovski M, Velte C, Bruckner BR, Alexopoulos I, Czopka T, Jung SY, et al. (2015). Actin filament turnover drives leading edge growth during myelin sheath formation in the central nervous system. Dev. Cell 34, 139–151. 10.1016/j.devcel.2015.05.013. [PubMed: 26166299]

Norrmen C, Figlia G, Lebrun-Julien F, Pereira JA, Trotzmuller M, Kofeler HC, Rantanen V, Wessig C, van Deijk AL, Smit AB, et al. (2014). mTORC1 controls PNS myelination along the mTORC1-RXRgamma-SREBP-lipid biosynthesis axis in Schwann cells. Cell Rep. 9, 646–660. 10.1016/j.celrep.2014.09.001. [PubMed: 25310982]

Ong HH, and Wehrli FW (2010). Quantifying axon diameter and intracellular volume fraction in excised mouse spinal cord with q-space imaging. Neuroimage 51, 1360–1366. 10.1016/j.neuroimage.2010.03.063. [PubMed: 20350604]

Ornelas IM, Khandker L, Wahl SE, Hashimoto H, Macklin WB, and Wood TL (2020). The mechanistic target of rapamycin pathway downregulates bone morphogenetic protein signaling to promote oligodendrocyte differentiation. Glia. 10.1002/glia.23776.

Perez-Cerda F, Sanchez-Gomez MV, and Matute C (2015). Pio del Rio Hortega and the discovery of the oligodendrocytes. Front. Neuroanat 9, 92. 10.3389/fnana.2015.00092. [PubMed: 26217196]

Perge JA, Niven JE, Mugnaini E, Balasubramanian V, and Sterling P (2012). Why do axons differ in caliber? J. Neurosci 32, 626–638. 10.1523/JNEUROSCI.4254-11.2012. [PubMed: 22238098]

Ramanan VK, Przybelski SA, Graff-Radford J, Castillo AM, Lowe VJ, Mielke MM, Roberts RO, Reid RI, Knopman DS, Jack CR, et al. (2018). Statins and brain health: alzheimer's disease and cerebrovascular disease biomarkers in older adults. J. Alzheimers Dis 65, 1345–1352. 10.3233/JAD-180446. [PubMed: 30149450]

Richter-Landsberg C (2008). The cytoskeleton in oligodendrocytes. Microtubule dynamics in health and disease. J. Mol. Neurosci 35, 55–63. 10.1007/s12031-007-9017-7. [PubMed: 18058074]

Rowitch DH, and Kriegstein AR (2010). Developmental genetics of vertebrate glial-cell specification. Nature 468, 214–222. 10.1038/nature09611. [PubMed: 21068830]

Saher G, Brugger B, Lappe-Siefke C, Mobius W, Tozawa R, Wehr MC, Wieland F, Ishibashi S, and Nave KA (2005). High cholesterol level is essential for myelin membrane growth. Nat. Neurosci 8, 468–475. 10.1038/nn1426. [PubMed: 15793579]

Saher G, Quintes S, and Nave KA (2011). Cholesterol: a novel regulatory role in myelin formation. Neuroscientist 17, 79–93. 10.1177/1073858410373835. [PubMed: 21343408]

Saher G, Rudolphi F, Corthals K, Ruhwedel T, Schmidt KF, Lowel S, Dibaj P, Barrette B, Mobius W, and Nave KA (2012). Therapy of Pelizaeus-Merzbacher disease in mice by feeding a cholesterol-enriched diet. Nat. Med 18, 1130–1135. 10.1038/nm.2833. [PubMed: 22706386]

Schaeren-Wiemers N, Bonnet A, Erb M, Erne B, Bartsch U, Kern F, Mantei N, Sherman D, and Suter U (2004). The raft-associated protein MAL is required for maintenance of proper axon–glia interactions in the central nervous system. J. Cell Biol 166, 731–742. 10.1083/jcb.200406092. [PubMed: 15337780]

Smolders I, Smets I, Maier O, vandeVen M, Steels P, and Ameloot M (2010). Simvastatin interferes with process outgrowth and branching of oligodendrocytes. J. Neurosci. Res 88, 3361–3375. 10.1002/jnr.22490. [PubMed: 20857509]

Sommer I, and Schachner M (1981). Monoclonal antibodies (O1 to O4) to oligodendrocyte cell surfaces: an immunocytological study in the central nervous system. Dev. Biol 83, 311–327. 10.1016/0012-1606(81)90477-2. [PubMed: 6786942]

Stuart T, Butler A, Hoffman P, Hafemeister C, Papalexi E, Mauck WM 3rd, Hao Y, Stoeckius M, Smibert P, and Satija R (2019). Comprehensive integration of single-cell data. Cell 177, 1888–1902.e1. 10.1016/j.cell.2019.05.031. [PubMed: 31178118]

Sturrock RR (1980). Myelination of the mouse corpus callosum. Neuropathol. Appl. Neurobiol 6, 415–420. 10.1111/j.1365-2990.1980.tb00219.x. [PubMed: 7453945]

Todorich BM, and Connor JR (2004). Redox metals in Alzheimer's disease. Ann. N. Y Acad. Sci 1012, 171–178. 10.1196/annals.1306.014. [PubMed: 15105264]

Tokumoto YM, Durand B, and Raff MC (1999). An analysis of the early events when oligodendrocyte precursor cells are triggered to differentiate by thyroid hormone, retinoic acid, or PDGF withdrawal. Dev. Biol 213, 327–339. 10.1006/dbio.1999.9397. [PubMed: 10479451]

Tyler WA, Gangoli N, Gokina P, Kim HA, Covey M, Levison SW, and Wood TL (2009). Activation of the mammalian target of rapamycin (mTOR) is essential for oligodendrocyte differentiation. J. Neurosci 29, 6367–6378. 10.1523/JNEUROSCI.0234-09.2009. [PubMed: 19439614]

Tyler WA, Jain MR, Cifelli SE, Li Q, Ku L, Feng Y, Li H, and Wood TL (2011). Proteomic identification of novel targets regulated by the mammalian target of rapamycin pathway during oligodendrocyte differentiation. Glia 59, 1754–1769. 10.1002/glia.21221. [PubMed: 21858874]

Varshney P, and Saini N (2018). PI3K/AKT/mTOR activation and autophagy inhibition plays a key role in increased cholesterol during IL-17A mediated inflammatory response in psoriasis. Biochim. Biophys. Acta Mol. Basis Dis 1864, 1795–1803. 10.1016/j.bbadis.2018.02.003. [PubMed: 29432814]

Vigano F, Mobius W, Gotz M, and Dimou L (2013). Transplantation reveals regional differences in oligodendrocyte differentiation in the adult brain. Nat. Neurosci 16, 1370–1372. 10.1038/nn.3503. [PubMed: 23995069]

Wahl SE, McLane LE, Bercury KK, Macklin WB, and Wood TL (2014). Mammalian target of rapamycin promotes oligodendrocyte differentiation, initiation and extent of CNS myelination. J. Neurosci 34, 4453–4465. 10.1523/JNEUROSCI.4311-13.2014. [PubMed: 24671992]

Wang J, Ho WY, Lim K, Feng J, Tucker-Kellogg G, Nave KA, and Ling SC (2018). Cell-autonomous requirement of TDP-43, an ALS/FTD signature protein, for oligodendrocyte survival and myelination. Proc. Natl. Acad. Sci. U S A 115, E10941–E10950. 10.1073/pnas.1809821115. [PubMed: 30373824]

Warrington AE, and Pfeiffer SE (1992). Proliferation and differentiation of O4+ oligodendrocytes in postnatal rat cerebellum: analysis in unfixed tissue slices using anti-glycolipid antibodies. J. Neurosci. Res 33, 338–353. 10.1002/jnr.490330218. [PubMed: 1453495]

Zhang Y, Chen K, Sloan SA, Bennett ML, Scholze AR, O'Keeffe S, Phatnani HP, Guarnieri P, Caneda C, Ruderisch N, et al. (2014). An RNA-sequencing transcriptome and splicing database of glia, neurons, and vascular cells of the cerebral cortex. J. Neurosci 34, 11929–11947. 10.1523/JNEUROSCI.1860-14.2014. [PubMed: 25186741]

Zuchero JB, Fu MM, Sloan SA, Ibrahim A, Olson A, Zaremba A, Dugas JC, Wienbar S, Caprariello AV, Kantor C, et al. (2015). CNS myelin wrapping is driven by actin disassembly. Dev. Cell 34, 152–167. 10.1016/j.devcel.2015.06.011. [PubMed: 26166300]

Highlights

- scRNA sequencing shows distinct oligodendrocyte precursors in brain and spinal cord
- Brain and spinal cord oligodendroglia differentially regulate cholesterol synthesis
- mTOR is necessary for normal cholesterol biosynthesis in oligodendroglia
- mTOR is necessary for myelin maintenance

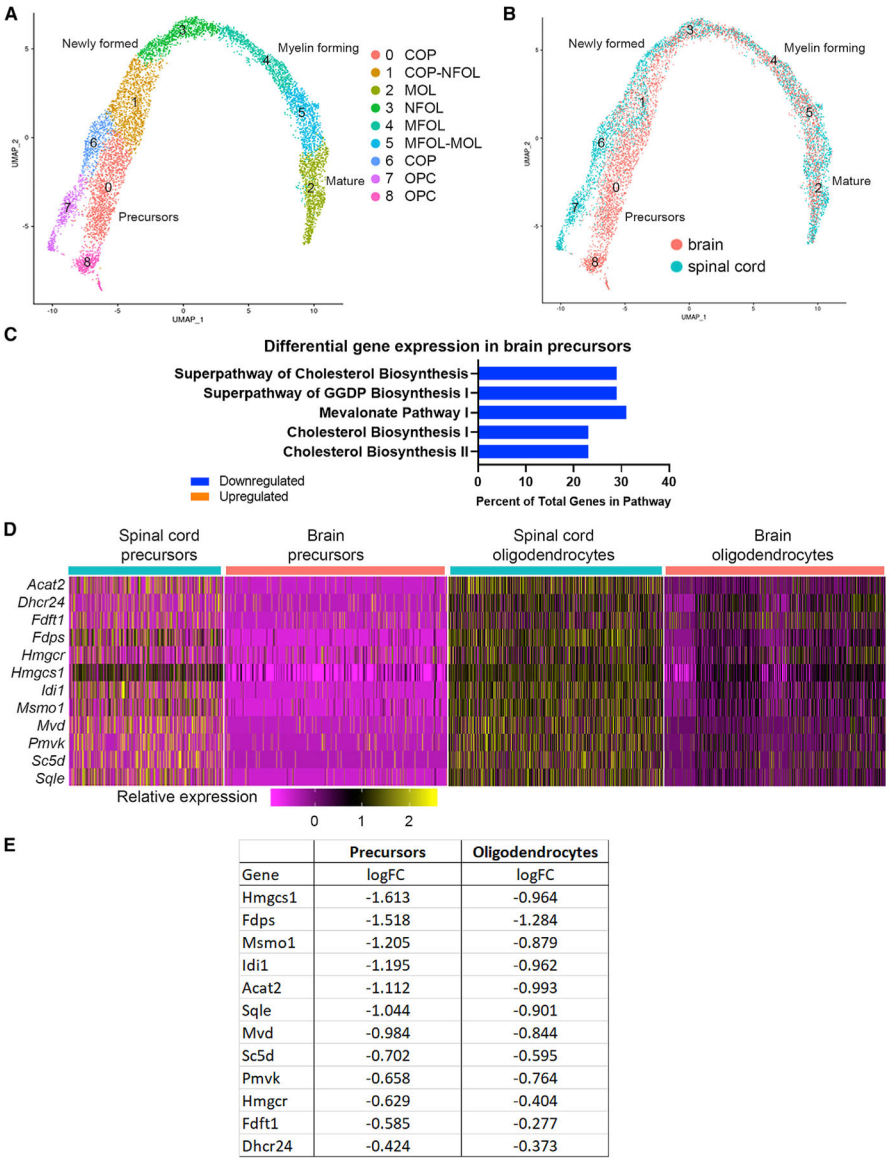

E

	Precursors	Oligodendrocytes
Gene	logFC	logFC
Hmgcs1	-1.613	-0.964
Fdps	-1.518	-1.284
Msmo1	-1.205	-0.879
Idi1	-1.195	-0.962
Acat2	-1.112	-0.993
Sqle	-1.044	-0.901
Mvd	-0.984	-0.844
Sc5d	-0.702	-0.595
Pmvk	-0.658	-0.764
Hmgcr	-0.629	-0.404
Fdft1	-0.585	-0.277
Dhcr24	-0.424	-0.373

Figure 1. Single-cell sequencing of O4$^+$ oligodendroglia from developing CNS reveals distinct populations in brain and spinal cord

Brain precursors have lower expression of cholesterol biosynthesis genes compared with spinal cord.

(A) UMAP of 8,208 integrated O4$^+$ oligodendroglia from developing brain (P14) and spinal cord (P10). Three littermates were pooled for brain; four littermates were pooled for spinal cord.

(B) O4$^+$ cells from brain (4,603 cells) and spinal cord (3,605 cells) cluster distinctly at precursor stages and overlap as they mature. Pink, brain; blue, spinal cord.

(C) Genes that were differentially expressed between brain precursors (clusters 8 and 0) and spinal cord precursors (clusters 7 and 6) were analyzed using IPA, and the top five global pathways identified are shown.

(D) Relative single-cell expression of the cholesterol biosynthesis genes differentially expressed between brain and spinal cord precursors and oligodendrocytes. Expression in

precursors is on the left (clusters 8, 7, 0, 6), and oligodendrocytes are on the right (clusters 1, 3, 4, 5, 2).

(E) Differential expression of cholesterol biosynthesis genes analyzed from single-cell data and presented as log fold change (logFC) in brain compared with spinal cord ($p < 0.0001$). Precursors (clusters 8, 7, 0, 6) and oligodendrocytes (clusters 1, 3, 4, 5, 2) are compared separately.

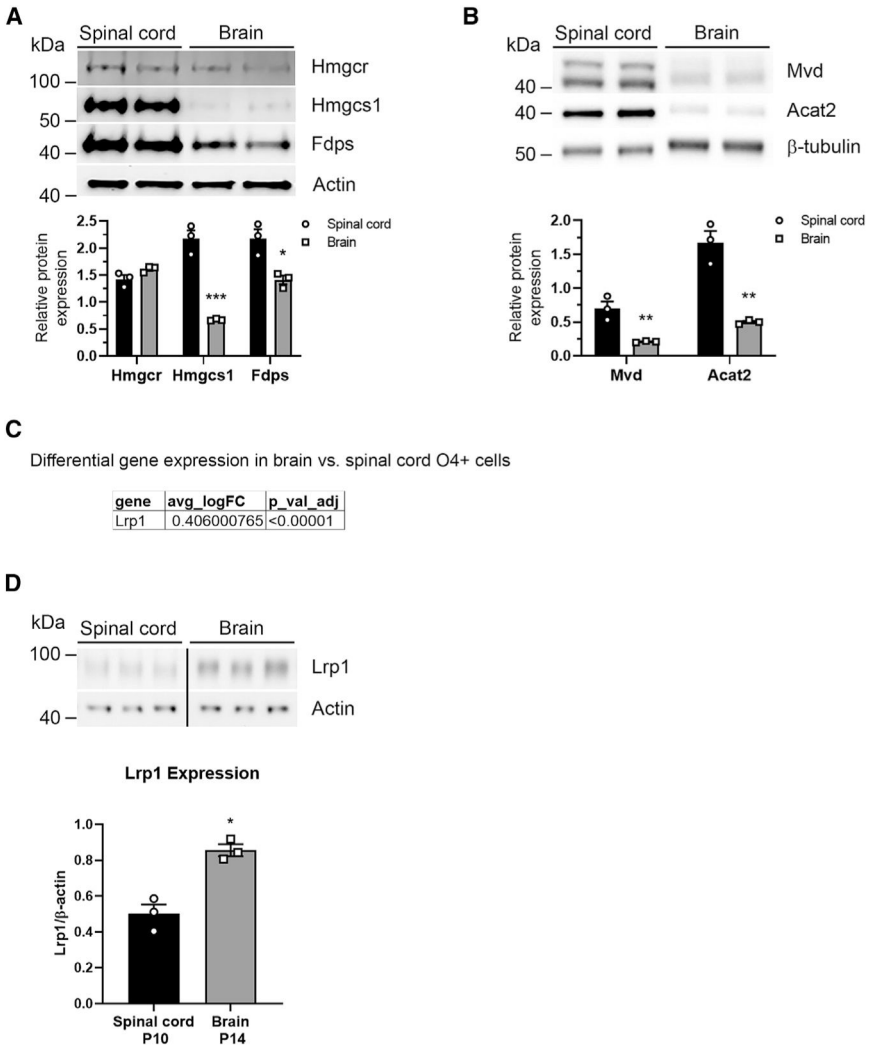

Figure 2. Brain and spinal cord oligodendroglia have different dependence on cholesterol synthesis and uptake

(A and B) Cell-autonomous cholesterol synthesis. Representative western blots showing expression of cholesterol biosynthesis enzymes HMGCR, HMGCS1, and FDPS (A) and MVD and ACAT2 (B) in $O4^+$ cells from P10 spinal cord and P14 brain. Data were quantified from three animals/genotype/CNS region. Values are expressed as the mean ± SEM.

(C and D) Receptor-mediated cholesterol uptake. Differential expression of *Lrp1* extracted from single-cell data and presented as logFC in all brain clusters compared with all spinal cord clusters (C). Representative western blots showing expression of the LRP1 in $O4^+$ cells from P10 spinal cord and P14 brain (D). Brain and spinal cord samples were run on the same western blot. For full image and additional time points see Figure S5D. Data were quantified from three animals/genotype/CNS region. Values are expressed as the mean ± SEM; *$p < 0.05$; **$p < 0.01$; ***$p < 0.001$.

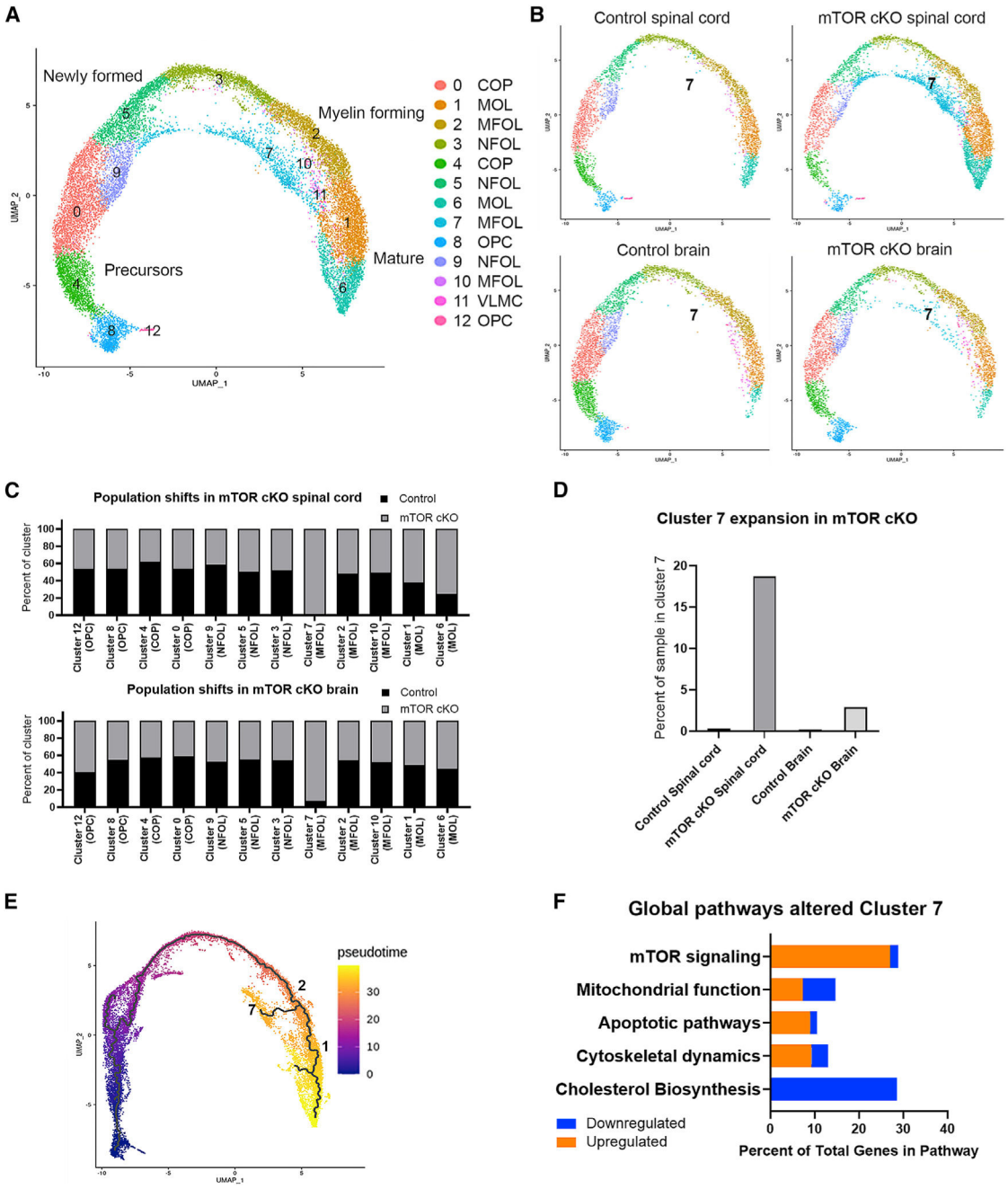

Figure 3. Oligodendroglial loss of mTOR results in expansion of a population with dysregulated global pathways

(A) UMAP plot of $O4^+$ cell clustering from integrated brain and spinal cord of control and mTOR cKO animals. The non-oligodendroglial vascular leptomeningeal cell (VLMC) cluster (cluster 11) was excluded from further analyses. OPCs in cluster 12 have a higher expression of cell-cycle genes, indicating that they are cycling cells. We assayed 8,208 control cells (3,605 from P10 spinal cord, 4,603 from P14 brain) and 9,120 mTOR cKO cells (5,233 from P10 spinal cord, 3,887 from P14 brain). Three littermates/genotype were pooled for brain; four littermates/genotype were pooled for spinal cord.

(B) UMAP plots separated by sample show that cluster 7 is present almost exclusively in mTOR cKO.
(C) Population shifts in mTOR cKO spinal cord and brain. The percentage of cells in each cluster that are control or mTOR cKO is shown.
(D) Percentage of each sample present in cluster 7. Control spinal cord, 0.3%; mTOR cKO spinal cord, 18.7%; control brain, 0.2%; mTOR cKO brain, 2.9%.
(E) Cells from integrated analysis with the Seurat package are ordered by pseudotime algorithms using the Monocle3 R package. The trajectory begins at OPCs in purple and progresses to MOLs in yellow.
(F) Top global pathways differentially expressed in cluster 7 compared with cluster 2, analyzed using IPA. Blue, downregulated genes; orange, upregulated genes.

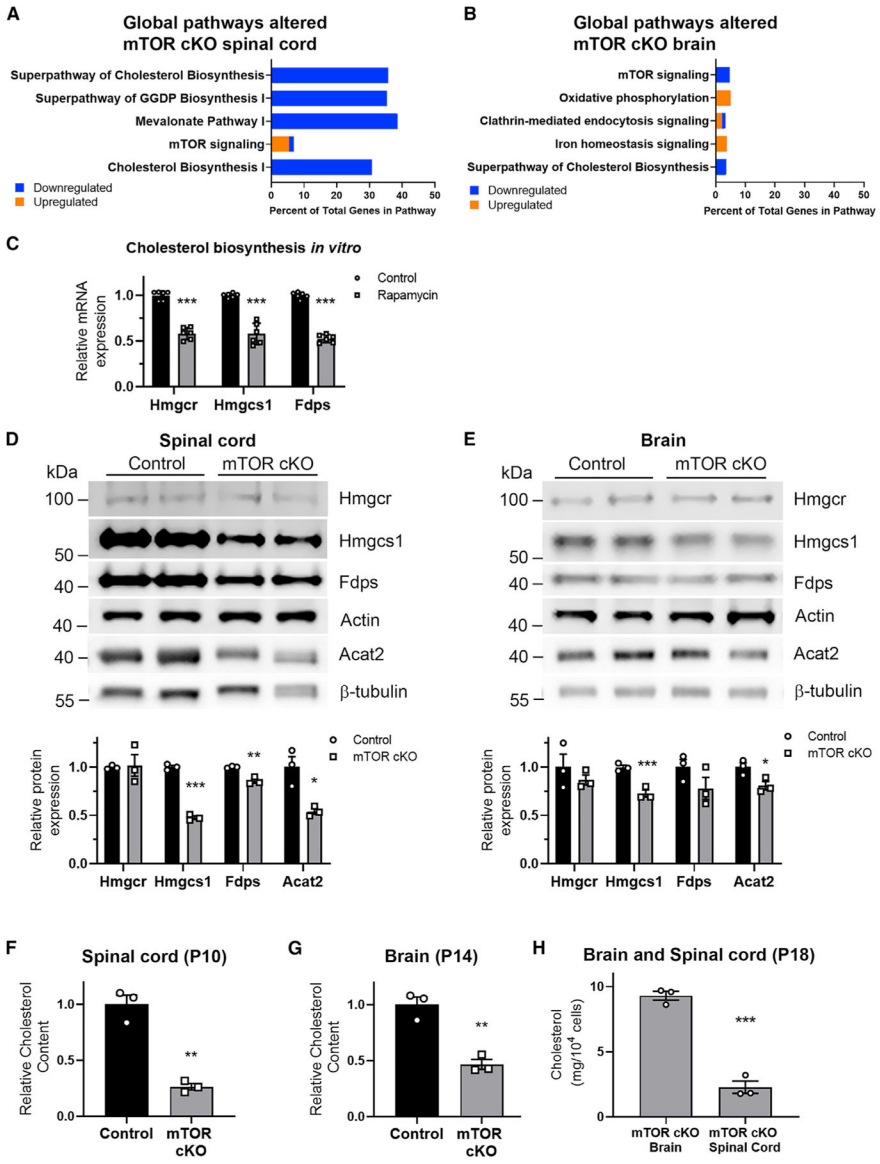

Figure 4. mTOR is necessary for normal cholesterol biosynthesis in oligodendroglia

(A and B) Top five pathways dysregulated in mTOR cKO spinal cord (A) and brain (B). IPA was done on genes differentially expressed in all mTOR cKO cells compared with all control cells; the most significantly altered pathways are shown. Blue, downregulated genes; orange, upregulated genes.

(C) Inhibiting mTOR *in vitro* reduces mRNA expression of cholesterol biosynthesis genes. Expression of *Hmgcr, Hmgcs1,* and *Fdps* by qRT-PCR in primary rat OPCs differentiated for 3 days in the presence or absence of 10 nM rapamycin to inhibit mTOR is shown. Expression was normalized to *Gapdh* as a housekeeping gene and then normalized to control. Data represent six replicates over two independent OPC preps. Values are expressed as the mean ± SD.

(D and E) Cholesterol biosynthesis enzymes are reduced in mTOR cKO spinal cord (D) and brain (E), with a greater impact in the spinal cord. Representative western blots

show expression of HMGCR, HMGCS1, FDPS, and ACAT2 in control and mTOR cKO spinal cord (D) and brain (E) $O4^+$ cells. HMGCR, HMGCS1, and FDPS expression was normalized first to β-actin and then to control. ACAT2 expression was normalized first to β-tubulin and then to control. Graphs present data from three animals/genotype/CNS region. Values are expressed as the mean ± SEM.

(F, G, and H) mTOR cKO $O4^+$ cells have lower cholesterol content. Total cholesterol measured in isolated $O4^+$ cells from P10 spinal cords (F), P14 brains (G), and P18 brains and spinal cords (H) and normalized to cell number. Graphs present data from three animals/genotype/CNS region. Values are expressed as the mean ± SEM. *$p < 0.05$; **$p < 0.01$; ***$p < 0.001$.

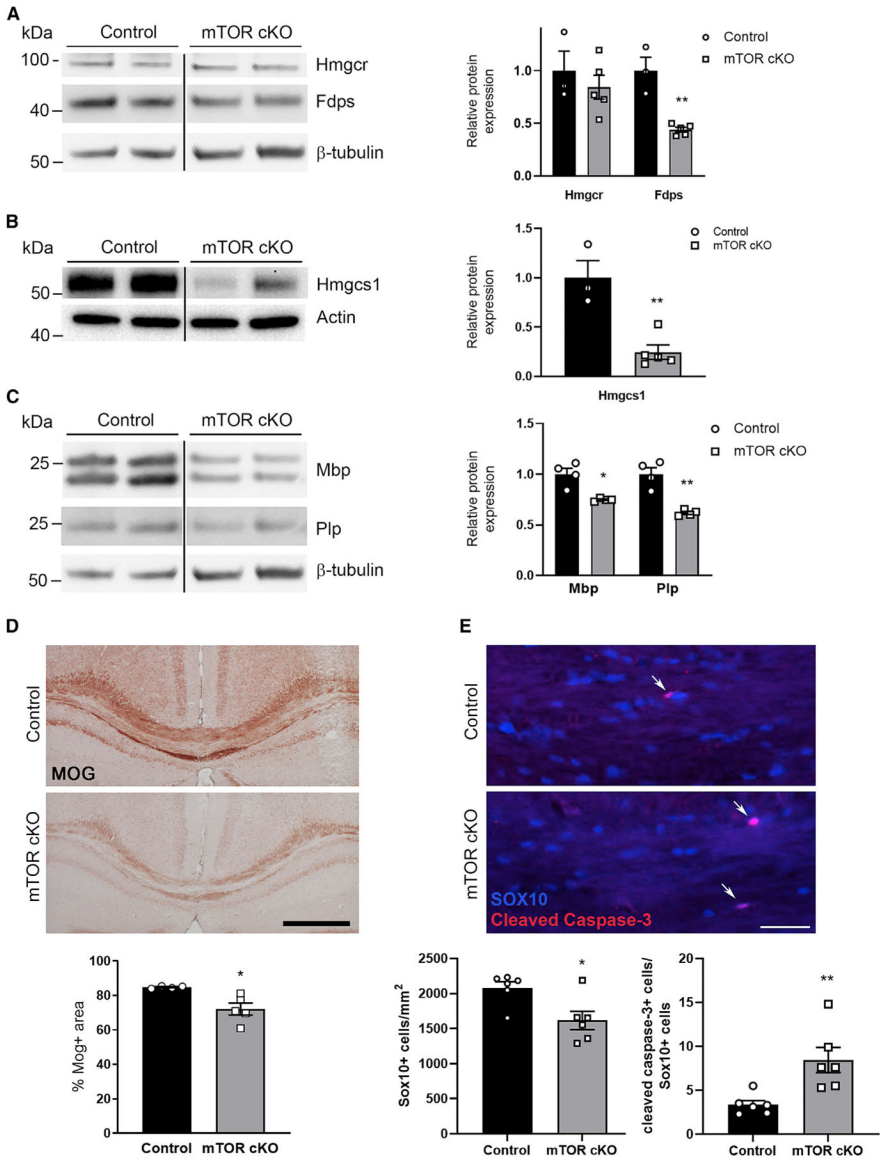

Figure 5. Deficits in cholesterol biosynthesis persist at 8 weeks of age, myelin protein expression is downregulated, and brain oligodendroglia undergo apoptosis

(A and B) Cholesterol biosynthesis enzymes are downregulated at 8 weeks in mTOR cKO corpus callosum. Representative western blots showing expression of HMGCR and FDPS (A) and HMGCS1 (B) in control and mTOR cKO microdissected corpus collosum. Graphs present data from three control and five mTOR cKO animals.

(C) Representative western blots showing expression of MBP and PLP in control and mTOR cKO microdissected corpus collosum at 8 weeks of age. Graph presents data from four control and four mTOR cKO animals. For (A), (B), and (C), control and mTOR cKO samples were run on the same western blot. Expression was normalized first to β-tubulin or actin and then to control. Values are expressed as the mean ± SEM.

(D) MOG expression is dysregulated in mTOR cKO corpus callosum. Representative images of MOG staining show area of positivity in corpus callosum. Scale bar, 500 μm. Graph

presents data from four control and five mTOR cKO animals. All values are expressed as the mean ± SEM.

(E) Representative images of SOX10 (blue, oligodendroglial marker) and cleaved caspase-3 (red, marker of apoptosis) immunostaining from control and mTOR cKO corpus callosum at 7–8 weeks of age. Scale bar, 50 μm. Arrows indicate cleaved caspase-3^+/$SOX10^+$ cells. Graphs present data from six animals/genotype. All values are expressed as the mean ± SEM. *$p < 0.05$; **$p < 0.01$.

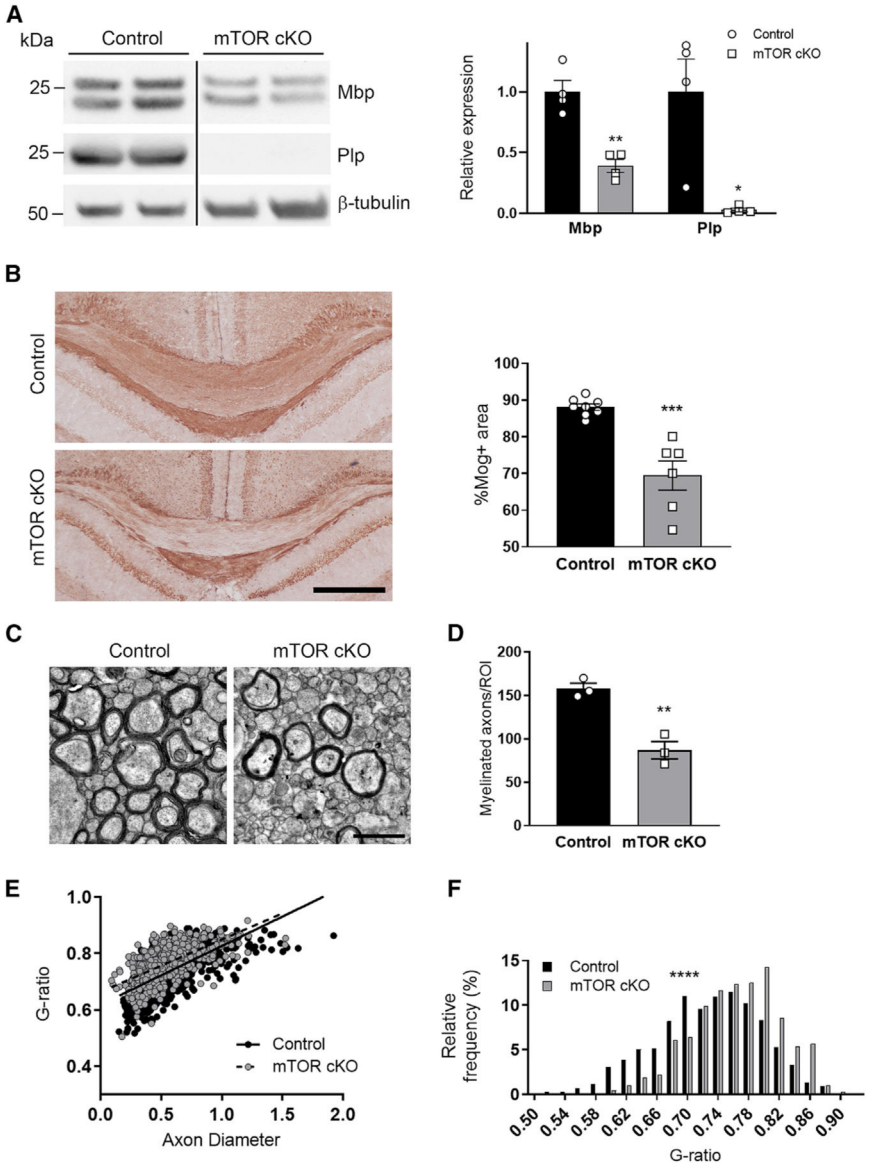

Figure 6. At 12 weeks, mTOR cKO brains exhibit dysregulation of myelin genes and hypomyelination

(A) Representative western blots showing decreased expression of MBP and PLP in mTOR cKO microdissected corpus collosum compared with control. Control and mTOR cKO samples were run on the same western blot. Expression of proteins was normalized first to β-tubulin and then to control. Graph presents data from four control and four mTOR cKO animals. All values are expressed as the mean ± SEM.

(B) MOG expression is dysregulated in mTOR cKO corpus callosum. Representative images of MOG staining show the area of positivity in corpus callosum. Scale bar, 500 μm. Graph presents data from eight control and six mTOR cKO animals. All values are expressed as the mean ± SEM.

(C) Demyelination apparent by 12 weeks in the corpus callosum of mTOR cKO mice. Representative EM images from 12-week control and mTOR cKO corpus callosum. Scale bar, 1 μm. All values are expressed as the mean ± SEM.
(D) Quantification of the number of myelinated axons in 12-week control and mTOR cKO callosa, n = 3/group.
(E) A g-ratio scatterplot showing linear regressions for 12-week control (solid) and mTOR cKO (dashed) g-ratios, slope $p = 0.048$, $n > 600$/group.
(F) The g-ratio distribution of 12-week control and mTOR cKO g-ratios, $n > 600$/group. *$p < 0.05$; **$p < 0.01$; ***$p < 0.001$; ****$p \leq 0.0001$.

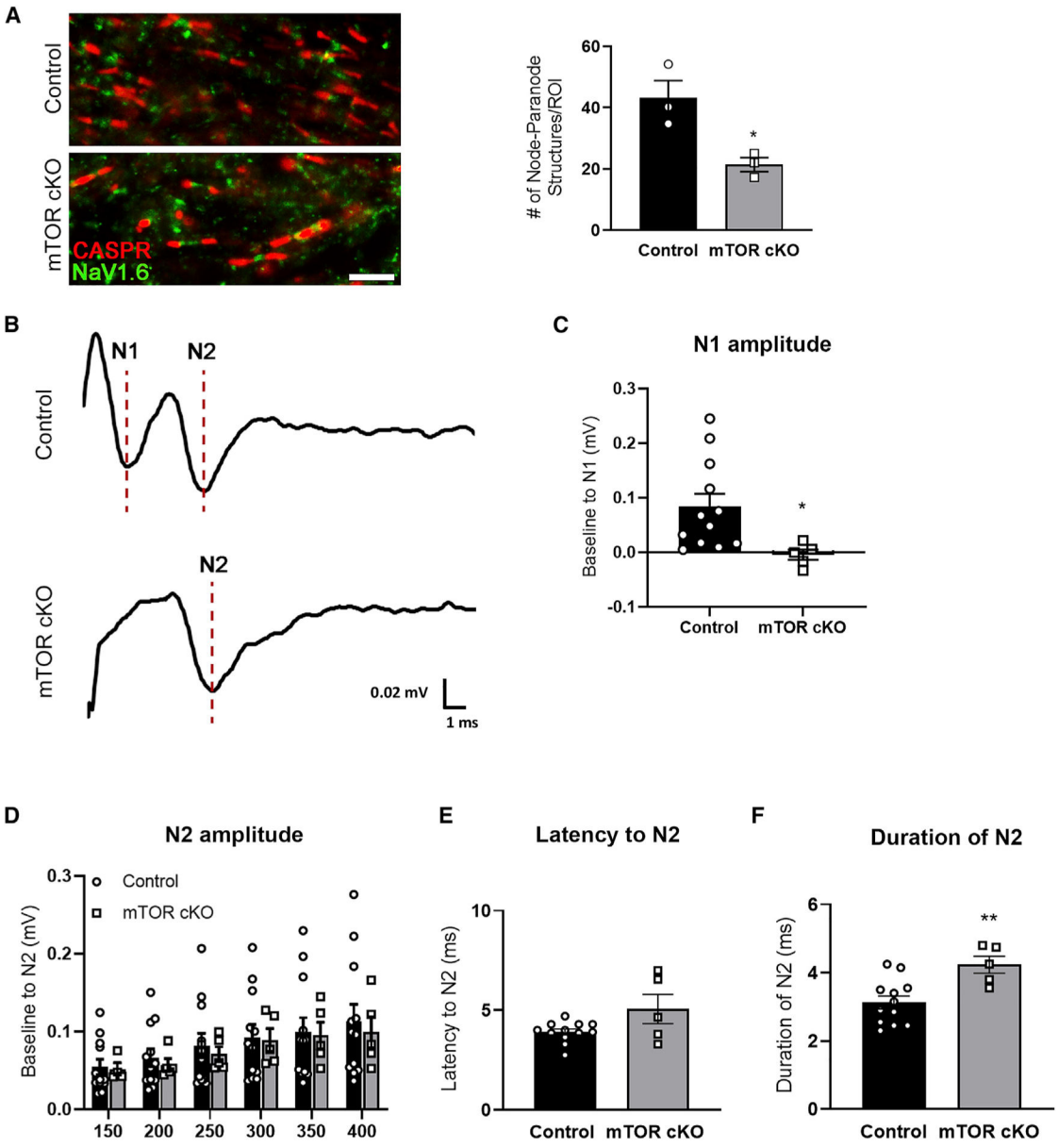

Figure 7. Developmental loss of mTOR disrupts nodal structures and axonal function in the adult corpus callosum

(A) Representative images of CASPR (red) and NaV1.6 (green) immunostaining in the 12-week control and mTOR cKO callosum. Scale bar, 5 μm. On the right is the quantification of the number of node-paranode structures (defined as CASPR-NaV1.6-CASPR) present in the midline callosum, n = 3/genotype. All values are expressed as the mean ± SEM.

(B–F) Axonal function in the corpus callosum of control and mTOR cKO at 13 weeks of age measured by compound action potential (CAP) callosal slice recordings. (B) Representative traces from CAP callosal slice recordings. N1, myelinated fiber response; N2, unmyelinated fiber response. (C) The amplitude of the N1 response at 400 μA stimulation intensity, n = 5–12/group. (D) The amplitude of the N2 response measured across increasing stimulation intensities, n = 4–12/group. (E) The latency to the N2 response at 400 μA stimulation

intensity, n = 5–12/group. (F) The duration of the N2 at 400 μA stimulation intensity, n = 5–12/group. For (C)–(F), all values are expressed as the mean ± SEM. *p < 0.05; **p < 0.01.

KEY RESOURCES TABLE

REAGENT or RESOURCE	SOURCE	IDENTIFIER
Antibodies		
O4-APC	Miltenyi	130-119-155; RRID: AB_2751644
Hmgcr	Invitrogen	PA5-37367; RRID:AB_2554032
Hmgcs1	Cell Signaling	42201S; RRID:AB_2799216
Fdps	Proteintech	16129-1-AP; RRID:AB_2104749
Lrp1	Abcam	ab92544; RRID:AB_2234877
β-actin	Sigma	A5441; RRID:AB_476744
β-actin	Cell Signaling	5125; RRID:AB_1903890
MBP	Covance	SMI-99; RRID:AB_2314772
PLP	Macklin Lab	N/A
β-tubulin	Cell Signaling	5346S; RRID:AB_1950376
β-amyloid	Invitrogen	51-2700; RRID:AB_87659
SMI-32	Biolegend	801701; RRID:AB_2564642
SOX10	R&D Systems	AF2864; RRID:AB_442208
Cleaved caspase-3	Cell Signaling	9664S; RRID:AB_2070042
MOG	Abcam	ab32760; RRID:AB_2145529
CASPR	Millipore	MABN69; RRID:AB_10806491
NaV1.6	Alomone Labs	ASC-009; RRID:AB_2040202
donkey anti-mouse 647	Life Technologies	A31571; RRID:AB_162542
donkey anti-goat AMCA	Jackson Laboratories	705-155-147; RRID:AB_2340409
donkey anti-rabbit 647	Life Technologies	A31573; RRID:AB_2536183
goat anti-mouse 647	Life Technologies	A21235; RRID:AB_2535804
biotinylated goat anti-rabbit	Vector Laboratories	BA-1000; RRID:AB_2313606
Goat anti-rabbit	Jackson ImmunoResearch	111-035-003; RRID:AB_2313567
Goat anti-mouse	Jackson ImmunoResearch	115-035-003; RRID:AB_10015289
Chemicals, peptides, and recombinant proteins		
FcR blocking reagent, mouse	Miltenyi	130-092-575; RRID:AB_2892833
Anti O4 microbeads	Miltenyi	130-094-543; RRID:AB_2847907
Rapamycin	Calbiochem	553210
Simvastatin	Millipore	567022
RIPA buffer	Thermo Scientific	89900
Halt Protease/Phosphatase Inhibitor Cocktail	Thermo Scientific	78440
Superscript II Reverse Transcriptase	Invitrogen	18064014
SYBR green detection master mix	BioRad	430001607
streptavidin-HRP	Pierce	21126
Fluorogel	Electron Microscopy Sciences	17985-10
2% PFA/2.5% glutaraldehyde	Polysciences, Inc	01909-100
Fetal Bovine Serum	Sigma Aldrich	F0926

REAGENT or RESOURCE	SOURCE	IDENTIFIER
L-glutamine	Corning	25-005-CI
Penicillin/Streptomycin	Gibco	15140-122
Poly D Lysine	Sigma Aldrich	P1024
d-Biotin	Sigma Aldrich	B4501
Insulin-transferrin-selenium	Gibco	4140-045
Progesterone	Sigma Aldrich	P8783
Putrescine	Sigma Aldrich	P5780
FGF Recombinant protein	R&D Systems	233-FB-025
Triiodothyronine	Sigma Aldrich	T-2877
Milk	ChemCruz	sc-2325
Tween20	Fisher	BP337
Bovine serum albumin	Sigma Aldrich	A6003
Critical commercial assays		
Neural Dissociation Kit (P)	Miltenyi	130-092-628
RC DC Protein Assay Kit II	BioRad	5000122
RNeasy Plus Mini Kit	Qiagen	74134
MTT cell viability assay	Abcam	ab211091
Chromium Single Cell 3′ GEM, Library & Gel Bead Kit v3	10X Genomics	PN-1000075
Cholesterol Assay	StanBio	1010-430
Deposited data		
Single Cell Sequencing Raw Data	GEO repository	Accession number- GEO: GSE190859
Experimental models: Organisms/strains		
Mouse: *mTOR$^{fl/fl}$/Cre−/−, mTOR$^{fl/fl}$/Cre+/−*	Wahl et al. (2014)	N/A
Rat: Sprague Dawley Female Timed Pregnancy	Charles River	400SASSD
Oligonucleotides		
Gapdh	Qiagen	QT00199633
Mbp	Qiagen	QT00199255
Mag	Qiagen	QT00195391
Plp1	Qiagen	QT00176414
Hmgcr	Qiagen	QT00182861
Hmgcs1	Qiagen	QT00183267
Fdps	Qiagen	QT00175574
β-actin	Qiagen	QT00193473
Software and algorithms		
Cell Ranger Version 3.0.2	10X Genomics	RRID:SCR_017344
Seurat package version 3.0.2 within R 3.6.0	Satija Lab	RRID:SCR_007322
The monocle3 version 0.2.1 within R 3.6.3	Cole-Trapnell Lab	RRID:SCR_018685